The primary volcanic aerosol emission from Mt Etna: size-resolved particles with SO 2 and role in plume reactive halogen chemistry

Tjarda J. Roberts, D. Vignelles, M. Liuzzo, G. Giudice, A. Aiuppa, M. Coltelli, G. Salerno, Michel Chartier, Benoît Couté, Gwenaël Berthet, et al.

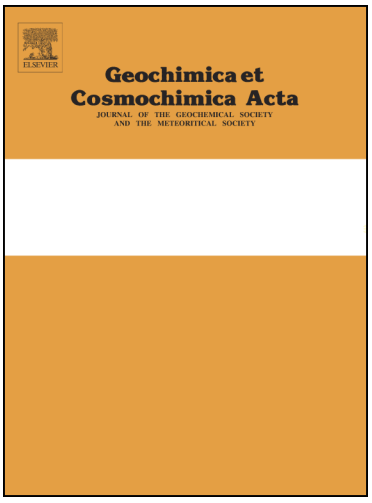

The primary volcanic aerosol emission from Mt Etna: size-resolved particles with SO_2 and role in plume reactive halogen chemistry

T.J. Roberts, D. Vignelles, M. Liuzzo, G. Giudice, A. Aiuppa, M. Coltelli, G. Salerno, M. Chartier, B. Couté, G. Berthet, T. Lurton, F. Dulac, J.-B. Renard

PII: S0016-7037(17)30629-4
DOI: https://doi.org/10.1016/j.gca.2017.09.040
Reference: GCA 10492

To appear in: *Geochimica et Cosmochimica Acta*

Received Date: 13 September 2016
Accepted Date: 23 September 2017

Please cite this article as: Roberts, T.J., Vignelles, D., Liuzzo, M., Giudice, G., Aiuppa, A., Coltelli, M., Salerno, G., Chartier, M., Couté, B., Berthet, G., Lurton, T., Dulac, F., Renard, J.-B., The primary volcanic aerosol emission from Mt Etna: size-resolved particles with SO_2 and role in plume reactive halogen chemistry, *Geochimica et Cosmochimica Acta* (2017), doi: https://doi.org/10.1016/j.gca.2017.09.040

The primary volcanic aerosol emission from Mt Etna: size-resolved particles with SO_2 and role in plume reactive halogen chemistry

T.J. Roberts[a]*, D. Vignelles[a], M. Liuzzo[b], G. Giudice[b], A. Aiuppa[c], M. Coltelli[d], G. Salerno[d], M. Chartier[a], B. Couté[a], G. Berthet[a], T. Lurton[a], F. Dulac[e], J.-B. Renard[a]

[a]LPC2E-CNRS/Université d'Orléans, 3A avenue de la recherche scientifique, 45071 Orléans, France

[b]Istituto Nazionale di Geofisica e Vulcanologia, sezione di Palermo, Via La Malfa 153, 90146 Palermo, Italy

[c]Dipartimento DiSTeM, Università di Palermo, Via Archirafi 36, 90123 Palermo, and Istituto Nazionale di Geofisica e Vulcanologia, sezione di Palermo, Via La Malfa 153, 90146 Palermo, Italy

[d]Istituto Nazionale di Geofisica e Vulcanologia, Osservatorio Etneo, Piazza Roma 2, Catania 95125, Italy

[e]LSCE-IPSL, CEA-CNRS-UVSQ, Université Paris-Saclay, CEA Saclay 701, 91191 Gif-sur-Yvette, France

[*]Corresponding author, Tjarda.Roberts@cnrs-orleans.fr

Abstract

Volcanoes are an important source of aerosols to the troposphere. Within minutes after emission, volcanic plume aerosol catalyses conversion of co-emitted HBr, HCl into highly reactive halogens (e.g. BrO, OClO) through chemical cycles that cause substantial ozone depletion in the dispersing downwind plume.

This study quantifies the sub-to-supramicron primary volcanic aerosol emission (0.2-5 µm diameter) and its role in this process. An in-situ ground-based study at Mt Etna (Italy) during passive degassing co-deployed an optical particle counter and Multi-Gas SO_2 sensors at high time resolution (0.1 Hz) enabling to characterize the aerosol number, size-distribution and emission flux.

A tri-modal volcanic aerosol size distribution was found, to which lognormal distributions are fitted. Total particle volume correlates to SO_2 (as a plume tracer). The measured particle volume:SO_2 ratio equates to a sulfate:SO_2 ratio of 1-2 % at the observed meteorological conditions (40% Relative Humidity). A particle mass flux of 0.7 kg s^{-1} is calculated for the measured Mt Etna SO_2 flux of 1950 tonnes/day.

A numerical plume atmospheric chemistry model is used to simulate the role of the hygroscopic primary aerosol surface area and its humidity dependence on volcanic plume BrO and OClO chemistry. As well as predicting volcanic BrO formation and O_3 depletion, the model achieves OClO/SO_2 in broad quantitative agreement with recently reported Mt Etna observations, with a predicted maximum a few minutes downwind. In addition to humidity – that enhances aerosols surface area for halogen cycling – background ozone is predicted to be an important control on

$OClO/SO_2$. Dependence of BrO/SO_2 on ambient humidity is rather low near-to-source but increases further downwind. The model plume chemistry also exhibits strong across-plume spatial variations between plume edge and centre.

Keywords

Particle, sulphate, halogen, impacts, volcano, atmospheric chemistry, troposphere, emission

Highlights

- In-situ small sensor quantification of Mt Etna primary aerosol emission
- Lognormal parameter fit finds trimodal primary aerosol, effective radius of 0.3 µm
- Data analysis of real-time observations extracts molar sulfate/SO_2 of 1-2 %
- Atmospheric model predicts OClO consistent with reported Mt Etna plume observations
- Aerosol surface area–humidity dependence of young plume BrO-OClO chemistry predicted

1. Introduction

Volcanoes release a complex and highly reactive cocktail of gases and aerosol to the atmosphere. Quiescent (passive) degassing contributes about ~40% of volcanic emissions, to the troposphere, whilst the remaining ~60% occurs by explosive eruptions to the troposphere or stratosphere (Halmer et al., 2002). This study focuses on the aerosol emissions and plume chemistry of Mt Etna (Italy) plume during continuous passive degassing.

Volcanic aerosols entering the troposphere impact climate through their effects on the earth's radiative balance (Schmidt et al., 2012, Ebmeier et al. 2014), are detrimental to the environment and health (Bussinger et al., 2015), and exert an important role in plume atmospheric chemistry: reactions on the acidic volcanic aerosol surface promote conversion of emitted volcanic halogens (HBr, HCl) into reactive halogens (e.g. BrO, OClO). Numerical models (MISTRA, *PlumeChem*) that simulate this plume chemistry predict depletion of tropospheric ozone (Bobrowski et al., 2007, Roberts et al., 2009, von Glasow et al., 2009), production of HNO_3 (Roberts et al., 2009), and conversion of mercury into a more toxic and easily deposited form (von Glasow, 2010). To date, volcanic BrO but not OClO has been reproduced by simulations of plume gas-aerosol chemistry, albeit with models only partially constrained.

Aerosol surface area is a key control on the near-source plume chemistry (Roberts et al., 2009, von Glasow, 2010) and depends on both the flux and size distribution of the primary volcanic aerosol emission. Several studies (see Section 1.1) have contributed towards characterising the sulphate-rich aerosol emission during passive degassing. Aircraft have also sampled explosive ash-rich and aged plumes (e.g. Schumann et al., 2011 Carn et al., 2011). However, the surface area of the primary sulphate-rich aerosol remains a key uncertainty in atmospheric models of plume chemistry and its impacts (Roberts et al., 2014a, Jourdain et al., 2015). This study quantifies the sub-to-supramicron primary volcanic aerosol emission using real-time in-situ aerosol and SO_2 sensors at quiescently

degassing Mt Etna volcano, and uses a numerical model to evaluate the role of humidity and aerosol surface area on plume BrO and OClO chemistry.

1.1 Volcanic aerosol observations

Volcanoes are a source of both primary and secondary aerosol to the atmosphere. A review is given by Mather et al. (2004a). Here the focus is on ash-poor emissions. Evidence for a primary aerosol emission comes from filter-pack sampling at the volcanic crater-rim (Mather et al., 2003, Mather et al., 2006), which identifies aerosol ions including SO_4^{2-}, i.e. sulfate aerosol. This is also confirmed by real-time chemical sampling, Kroll et al. (2015).

Primary volcanic aerosol includes components either directly released or formed over seconds-minutes timescale since release of the hot gas mixture from the vent. This contrasts with secondary sulfate aerosol that is formed by atmospheric oxidation of SO_2 over typically hours to days. Thermodynamic models (e.g. Martin et al., 2006) indicate H_2SO_4-precursors (e.g. SO_3, OH) are formed at high-temperature near to the vent. These are a possible source of primary sulfate. However, this high-temperature region of the plume is difficult to observe in the field, and its representation using models has known caveats (e.g. Martin et al., 2009, Martin et al., 2012, Roberts et al., 2014a). Therefore the mechanisms are uncertain. Nevertheless, plume observations made at ambient temperature e.g. of HO_2NO_2 (a product of HO_x and NO_x) at Mt Erebus (Oppenheimer et al., 2010) do provide some evidence for high-temperature production of oxidised gas radicals. As the near-vent plume cools, reaction of SO_3 with H_2O (ubiquitous in the volcanic emission) could lead to a rapid production of gaseous $H_2SO_{4(g)}$ that is highly hygroscopic and will therefore form aqueous $H_2SO_{4(aq)}$ particles upon plume cooling. Particles might also be directly released. Ammann and Burtscher (1993) propose that nanometer-sized metal salts may seed sulfate particle formation, with subsequent growth by H_2SO_4 condensation and particle coagulation. Reaction of H_2SO_4 with metal-chloride salts can partially neutralise the aerosol acidity, releasing metal ions such as $Na^+_{(aq)}$ (e.g. Martin et al., 2008) and HCl gas (Mather et al., 2004a). The result is a primary volcanic aerosol emission to the troposphere that is multi-modal in its size distribution (e.g. Allen et al., 2006). Sulfate is commonly a dominant component by mass but the aerosol emission can contain other ions (e.g. Quisefit et al., 1988; Toutain et al., 1995) or can atypically be halogen-rich, Ilyinskaya et al., (2010).

Volcanic aerosol can be characterised by (i) in-situ time-averaged sampling with laboratory analysis, (ii) remote sensing such as by sun-photometer and (iii) in-situ real-time sensing by optical particle counter (OPC). Previous aerosol studies at Mt Etna are listed in **Table 1** (remote sensing) and **Table 2** (in situ) and the three methods discussed below.

In-situ time-averaged sampling by filter-pack or cascade impactor (that separates the collected aerosol according to size) is reported by Vié le Sage (1983), Quisefit et al. (1988), Toutain et al. (1995), Allen et al. (2006) and Martin et al. (2008), finding high sulfur or sulfate content alongside other ions including metals, e.g. Na^+. Allen et al. (2006) report that sulfate was mostly in coarse particles at North-east crater (NEC) but in fine particles at Voragine (VOR), confirmed by Martin et al. (2008) who report sulfate with either single or bi-modal distributions, centred at ~1 µm (at VOR and NEC) and ~8 µm diameter (NEC only). Martin et al. (2008) report sulfate:SO_2 molar ratios from summit filterpack sampling of 0.017 - 0.05 and silica particles of ~ 1 µm with a flux of ~7000 kg d^{-1}.

Sun-photometer remote sensing by Watson and Oppenheimer (2000; 2001) quantified aerosol over 0.1-4 μm radius finding at least two size modes, an effective radius (R_{eff}) of ~0.7-0.85 μm and some evidence for particle growth downwind. However, surface area and volume were constrained only as lower limits as the distribution maxima lie beyond the retrieval range. A lower limit for the particle mass flux was given as 4.5-8 kg s^{-1}. An airborne multispectral (visible + infra-red) imaging study by Spinetti and Buongiorno, (2007), also indicated likely presence of multiple size modes, an effective radius of ~1 μm, but reported shrinkage of average particle size downwind (perhaps a consequence of the instrument size-range combined with aerosol microphysics). Sellito et al. (2016) detected aged aerosol by sun-photometer hundreds of km downwind from Mt Etna following an eruption event, reporting a bi-modal distribution, suggested to be sulfate (fine mode) and ash (coarse). Analysis of explosive events from Mt Etna observed by the MISR (Multiangle Imaging SpectroRadiometer) satellite instrument have also identified larger ash particles with finer sulfate-water particles (Scollo et al., 2012). Other studies have identified volcanic ash from satellite data but are not discussed here.

From real-time OPC measurements of aerosol number distribution at Mt Etna, Allen et al. (2006) report a trimodal distribution, with distinct NEC and VOR composition. However, surface area and volume distributions were not analysed. In the first application of an OPC to Mt Etna, Allen et al. (2006) emphasize the future potential application of OPC's alongside in-situ SO_2 gas sensors to deliver aerosol:SO_2 ratios, whose combination with SO_2 flux measured by UV remote sensing techniques such as COSPEC and DOAS (Differential Optical Absorption Spectroscopy) (Platt and Stutz, 2008) would enable a more accurate calculation of aerosol emission flux. Co-measurement of SO_2 would also enable the volcanic aerosol component to be distinguished from other sources e.g. dust. This approach is used here. We note that previous in-situ field-measurements of near-source Mt Etna aerosol alongside SO_2 found the OPC suffered from non-quantitative counting, preventing an accurate measurement (Vance et al., 2010). Here we trace and minimise such errors. Finally, in-situ measurements of aerosol in plume >6km downwind from Mt Etna have recently also been made by aircraft, reporting R_{eff} = 0.75-1.2 and porosity (aerosol with air-holes) at the observed low ambient temperature and humidity (Shcherbakov et al., 2016).

These studies collectively demonstrate a sulfate-rich primary volcanic aerosol emission from Mt Etna but exhibit differences that include: single, bi- or tri-modal distributions, supra- or sub-micron volumic maxima, growth or shrinkage downwind. These differences may reflect particular meteorological/volcanological conditions or measurement limitations. There remains a need to further characterise the primary aerosol emission, whose surface area exerts an important role in plume atmospheric chemistry.

1.2 The importance of volcanic aerosol in driving plume BrO, OClO chemistry

Volcanic aerosol catalyses plume chemical reactions that convert volcanic emissions of HBr and HCl into reactive halogens (e.g. BrO, OClO). Impacts from this plume chemistry include substantial depletion of ozone, as both predicted by atmospheric models (Von Glasow, 2009, Roberts et al., 2014a, and references therein) and observed (Vance et al., 2010, Schumann et al., 2011, Kelly et al. 2013, Surl et al., 2015). Important features of the volcano plume reactive halogen chemistry are

summarised in Figure 1. The chemistry occurs through autocatalytic cycles, the so-called "bromine explosion", involving gas-aerosol, gas-phase and photolytic reactions R1-R6, where X is a halogen Br or Cl. In strong (highly concentrated) plumes, additional Br-mediated ozone depletion is caused by the cycle between R4 and R7. The onset of the low-temperature tropospheric chemistry cycles in the downwind plume is 'kick-started' by high-temperature near-vent formation of radicals and sulfate aerosol precursors.

R1 $BrONO_{2(g)} + H_2O_{(aq)} \xrightarrow{aerosol-surface} HOBr_{(g)} + HNO_{3(aq,g)}$

R2 $HOBr_{(g)} + HX_{(aq)} \xrightarrow{aerosol-surface} BrX_{(g)} + H_2O_{(aq)}$

R3 $BrX_{(g)} \xrightarrow{sunlight} Br_{(g)} + X_{(g)}$

R4 $Br_{(g)} + O_{3(g)} \rightarrow BrO_{(g)} + O_{2(g)}$

R5 $BrO_{(g)} + HO_{2(g)} \rightarrow HOBr_{(g)} + O_{2(g)}$

R6 $BrO_{(g)} + NO_{2(g)} \rightarrow BrONO_{2(g)}$

R7 $BrO_{(g)} + BrO_{(g)} \rightarrow 2Br + O_{2(g)}$

Understanding BrO as a proxy for volcanic HBr emissions is a strong interest at Mt Etna, Italy, where BrO is frequently measured and OClO has also been observed (Bobrowski et al., 2007; Bobrowski and Guiffrida, 2012; General et al., 2014; Gliß et al., 2015). Unexpectedly, BrO/SO_2 at Mt Etna showed no observable dependence on relative humidity (RH) despite expectations to the contrary given high RH should enhance the hygroscopic volcanic aerosol surface area, promoting R1, R2 (Bobrowski and Guiffrida, 2012). This issue is investigated through modelling in this study.

Critical to the bromine explosion cycle are the heterogeneous (gas-aerosol) reactions (R1, R2) on the acidic aerosol surface area. The product of aerosol-catalysed reaction R2 is initially Br_2 (X = Br) for a typical volcanic emission composition such as at Mt Etna, see Roberts et al. (2014a). This leads to a rapid conversion of volcanic HBr into reactive bromine species including BrO. As the plume HBr becomes depleted the R2 reaction can instead release BrCl, that photolyses to generate Br and Cl radicals (R3), leading to formation of ClO and OClO by R8-R9.

R8 $Cl_{(g)} + O_{3(g)} \rightarrow ClO_{(g)} + O_{2(g)}$

R9 $ClO_{(g)} + BrO_{(g)} \rightarrow OClO_{(g)} + Br_{(g)}$

This proposed mechanism is of interest regarding OClO recently reported in Mt Etna plume (Bobrowski et al., 2007; General et al., 2015, Gliß et al., 2015). Volcanic OClO has also been reported in the tropospheric plume of Soufrière Hills (Donovan et al., 2014), and the stratospheric plume of Puyehue-Cordón Caulle (Theys et al., 2014). Observations of volcanic OClO have not been reproduced by atmospheric models to date, but are simulated here for Mt Etna using a box model (Section 4.2). Predicted impacts of the plume reactive chlorine chemistry include enhancing BrO-

induced ozone depletion and mercury deposition, and shortening of the lifetime of key climate gas methane through reaction with Cl radicals (Gliß et al., 2015, Jourdain et al., 2016).

2. Methods

During our field-campaign, 2-4 October, 2013, Mt Etna was quiescently degassing from three summit craters: North East Crater (NEC), Voragine (VOR), Bocca Nuova (BNC), these last two also known as Central Craters (CC), with no visible evidence for ash in their plumes. The OPC aerosol and Multi-Gas instruments were deployed as close to each other as possible (typically 10's cm) to facilitate direct in-situ comparison of the real-time (1-10's s) measurements. On 2 October, summit measurements were made at VOR, NEC and BNC consecutively. Strong winds occurred from an unusual north-westerly direction, also confirmed by meteorological balloon soundings in Trapani that indicate ~12 m s^{-1} (see http://weather.uwyo.edu/upperair/sounding.html). This allowed the plume to be traced for several hundred meters along the volcano flank as a descent was made from BNC by foot towards Torre del Filosofo (Figure 2). Near-downwind grounding plume was then sampled ~1.5 km (~2 minutes plume travel) south-east from the summit. On 4 October, under similar wind conditions the instruments were co-deployed again at this near-downwind location.

2.1 LOAC Optical Particle Counter and particle size distributions

The LOAC (Light Optical Aerosol Counter) instrument operated is a new lightweight (<1 kg) OPC (Renard et al., 2016). Version 1.1 was used here. It detects scattered light from a laser (650 nm) at low angle ~12 degree channel, whose signal is mostly independent of particle composition (Lurton et al., 2014). As well as the low angle channel used for particle counting and size attribution, the LOAC contains a second ~60 degree channel whose comparative signal can provide insight to the dominant particle nature in various size bins. This aspect is presented in Supplementary Material. Particles are counted and categorised according to scattered intensity into 19 size-bins between 0.2 and 50 (up to ~100) µm diameter. The airflow is drawn through the instrument inlet by a miniature pump ~2 L min^{-1} (flow rate verified before and after each field deployment). The data acquisition rate is ~0.1 Hz. A noise control and dark current calibration is performed each 15 min. Power was supplied by battery (replaced every few hours), and data logged to SD memory cards. Renard et al. (2016) report estimates of LOAC measurement uncertainties (1σ) in total number concentration due to stability of pump flow (±5%), laser (±5%), and detectors (±5%). In addition, size-calibration uncertainties are reported as ±0.025 µm for particles of size <0.6 µm, 5% for 0.7–2 µm, and 10% for particles >2 µm. Renard et al. (2016) report a standard deviation of ±15% (1σ) in number concentration for total particles <10 µm when LOAC instruments are co-deployed over ten minutes. Poisson statistics on particle counting are ±6% for particle concentrations > 1 cm^{-3}. Additional uncertainties can occur for particles <1 µm at low particle counts (when signal is close to the detection limit) but such conditions are not expected in the aerosol-rich volcanic plume. Conversely, measurement coincidence errors can occur at too high particle count as shown in Section 3.3. Optimal weak-plume data is selected (and averaged) in the subsequent analysis (Section 3.4). For total integrated area and volume we assume an error-bar of ±50% (Section 4.1).

The LOAC measurements were fitted to lognormal particle size distributions using a least-squares procedure. We choose to fit a lognormal distribution, commonly used in atmospheric models: it enables to relatively simply interconvert number, area and volume, and to estimate effective radius across the whole distribution, even beyond the instrument measurement range. The best results were obtained with three modes, consistently with reported size distributions (Martin et al., 2008; see section 3.4). Equations for the lognormal aerosol distribution and effective radius are given in Appendix A3.

2.2 Multi-Gas Instruments

Two Multi-Gas instruments were deployed alongside the LOAC to measure SO_2 mixing ratio (in ppmv, equivalent to μmol mol^{-1}) using three electrochemical sensors, and recorded other meteorological parameters. A direct exposure Multi-Gas (Roberts et al., 2017, based on Roberts et al., 2012), contained SO_2 sensor versions SO2-A4 and SO2-AE, manufactured by Alphasense Sensor Technology Company, Ltd, with reported rms noise <1.5 ppmv for SO2-AE and 15 ppbv for SO2-A4 (±2σ). The instrument used low noise electronics (3 mV peak-to-peak) with the sensor output (0 to 2.5 V) logged at 1-0.1 Hz using HOBO U12-006 datalogger (accuracy ±2 mV ±2.5% of absolute reading, precision 0.6 mV). The SO2-A4 has higher sensitivity (348 nA per ppmv) than SO2-AE (72 nA per ppmv) as determined by room-temperature pre-fieldwork calibrations, thus yields better resolution data (and stability). But it exhibits a lower range (~6 ppmv) compared to SO2-AE (~38 ppmv), for the electronics board used. Thus, the SO2-A4 sensor is most accurate for the study of dilute plumes. The co-deployment of multiple SO_2 sensors nevertheless provides opportunity for Multi-Gas intercomparison, see Supplementary Material. Temperature next to the sensors (close to ambient given no instrument heating) was monitored using a PT1000 resistance thermometer. Electrochemical sensor sensitivities are temperature dependent but at the ambient field-temperatures encountered (10-15˚C) the sensor sensitivity is within 3% of the calibrations (at 20˚C) according to Alphasense specifications. A second Multi-Gas, with pumped design similar to that described by Shinohara et al. (2008), was co-deployed and contained another electrochemical sensor for SO_2 (version 3ST/F, manufactured by City Technology, range 0-200 ppmv, repeatability 1%, resolution 0.1 ppmv), and pressure and humidity sensors. Data were stored on a data-logger specifically designed by INGV-Palermo, able to sample at a frequency of 0.5 Hz. The H_2O measurement was determined as a function of P, T and RH as suggested by the Buck (1981) equation, E1, where *T* is the temperature (˚C), *RH* the relative humidity (percent), and P the pressure (hPa).

E1 $$[H_2O_{(g)}] = 6.1121 \cdot \left(1.0007 + 3.46 \cdot 10^{-6} \cdot P\right) \cdot Exp\left[\frac{17.502 \cdot T}{240.97 + T}\right] \cdot 10^4 \cdot RH \cdot P^{-1}$$

2.3 *PlumeChem* model of plume BrO and OClO chemistry

The *PlumeChem* box model (Roberts et al., 2009, 2014a) simulates the reactive halogen atmospheric chemistry of a dispersing plume in the troposphere, in a Lagrangian-type approach. The model

includes detailed halogen chemistry (species: BrO, Br, HBr, $BrONO_2$, HOBr, BrCl, $BrNO_2$, BrNO, BrONO, Cl, HCl, ClO, OClO, $ClONO_2$, HOCl) as well as a background atmospheric scheme, with gas-phase, photolytic and heterogeneous (gas-aerosol) reactions. The $BrNO_2$ chemistry follows Roberts et al. (2014a), with less $BrNO_2$ accumulation than Von Glasow (2010). The model initialisation around midday injected volcanic gases to an altitude of ~3.5 km. Ambient temperature was 285 K and wind-speed set to 10 m s^{-1}. Plume dispersion followed Pasquill-Gifford case C (Davidson et al., 1990). This is applicable for wind-speeds >6 m/s with strong insolation, or wind-speeds 3-6 m/s with weak-moderate insolation. Both scenarios yield similar near-source plume BrO/SO_2 (Roberts et al., 2014a), although plume-air mixing is a source of uncertainty in the model chemistry, see Section 4.2. The simulated Mt Etna emission included H_2O, CO_2, HCl, SO_2, H_2S, HBr following Roberts et al. (2014a), with an SO_2 flux of around 20 kg s^{-1}. The emitted HBr/SO_2 = 4.8×10^{-4} (7.4×10^{-4} in sensitivity study) was close to that recently reported at Etna BN crater by Wittmer et al. (2014), although it is noted that Mt Etna HBr emissions may be variable (Bobrowski and Guiffrida, 2012). This emission was modified to account for near-vent high-temperature chemistry using the HSC thermodynamic model to generate radicals including OH, Cl, Br, NO_x and SO_3. A 5:95 atmospheric:magmatic gas mixture was used, assuming 1050 ˚C magmatic temperature, see Roberts et al. (2014a) for tabulated Mt Etna emission and HSC output. This was followed by a further rapid dilution to crater-rim SO_2 (tens of ppmv). Aerosol surface area was specified independently in the model initialisation as a function of humidity. The model was used to simulate near-source plume chemistry evolution over 20-30 min. In single box mode mixing of background air is provided at 10s intervals by entrainment from a second box. Single box mode was used to simulate plume evolution for a range of background ozone (30-100 ppbv) and relative humidity (10-90%). Multi-grid-box mode was used to provide horizontally spatially resolved plume composition for the two HBr/SO_2 emission ratios: in this setting, plume dispersion is simulated every 10 s across 130 grid-boxes of 38 m horizontal resolution, which expand in the vertical as air is entrained. For computational efficiency a half plume is simulated and reflected in a vertical plane of symmetry to yield the whole plume chemical composition. See Kelly et al. (2013) for a previous demonstration of this approach.

3. Results: quantifying the primary volcanic aerosol emission from Mt Etna

3.1 High resolution time-series of aerosol volume co-measured with SO_2

Time-series of total aerosol volume co-measured with SO_2 (Figure 3) show high plume exposures at the three summit craters VOR, NEC and BNC (SO_2 up to ~35 ppmv, causing the SO2-A4 sensor to saturate but detected by SO2-AE). As the descent was made along the flank into weaker (more dilute) plume, both the aerosol volume and SO_2 decline. This confirms the volcanic aerosol source. Episodes of very high aerosol also occur especially during the descent by foot. These are not correlated to SO_2. They are most likely resuspended dust generated during the descent, which could also be seen visually. Data were selected to minimise this dust contamination; the period (02 Oct 14:03-14:43) is labelled 'Flank'. Very weak plume was subsequently measured at ~1.5 km downwind (see Figure 4 for details) with a dust-free period (02 Oct 16:13-16:36) labelled 'Vweak'. On 04 October, further near-downwind measurements were made (Figure 5) with two largely dust-free periods labelled 'DW1' (04 Oct 14:18 – 15:28) and 'DW2' (04 Oct 15:30 – 16:12), respectively (separated by an OPC instrument restart). These four time-periods (especially Vweak) form the basis

for further analysis of the bulk plume. The individual crater-rim observations are not analysed in detail given probable OPC coincidence errors, see Section 3.3.

3.2 Correlation in aerosol volume and SO_2 and derivation of sulfate:SO_2 ratios

The strong correlation between measured total aerosol volume and volcanic SO_2 is further shown by a scatter plot of the Vweak, Flank, DW1 and DW2 data (Figure 6). A least-squares linear regression on the Vweak data-set (R^2 = 0.6) finds gradient 64.8 μm^3 cm^{-3} per ppmv SO_2 with intercept 2.2 μm^3 cm^{-3}. This regression line appears consistent with the Flank data, noting occasional dust episodes that elevate total volume. The regression line is also reasonably consistent with DW1 and DW2 datasets, although these exhibit more noisy signals in the smaller size bins, causing a volume offset at low particle number.

Our in-situ co-measurement of aerosol and SO_2 enables further analysis of the real-time data to derive sulfate:SO_2 ratios. The approach converts measured aerosol volume into sulfate concentration using the hygroscopic property weight-percent (wt%) sulfate that is a strong function of humidity. We assume pure $H_2SO_{4(aq)}$ or $NaHSO_{4(aq)}$ composition, deduced from reported time-averaged sampling of Mt Etna aerosol (ash-poor conditions) by Martin et al. (2008). Parameterisations of wt% sulfate and aerosol density as a function of humidity and temperature determined the $H_2SO_{4(aq)}$ molar volume (**Table 3**). This was used to convert measured aerosol volume into sulfate molar content (**Table 4;** see Appendix A1, A2) hence sulfate:SO_2 ratios (as SO_2 was co-measured). The observed 64.8 μm^3 aerosol per ppmv SO_2 during the Vweak period (measured at 1.83 10^{19} molec.cm^{-3}, 11.9 ˚C and 38% RH) equates to a sulfate:SO_2 molar ratio of 0.01-0.02. This magnitude is consistent with reported filter-pack SO_4^{2-}:SO_2 ratios (0.017, 0.049, 0.05 mol mol^{-1}) at Mt Etna (Martin et al., 2008), with ~1:100 typical at the volcano crater-rim (e.g. Mather et al., 2003). Also shown in **Table 4** is a further sulfate:SO_2 calculation based on selected data that minimises coincidence errors (see Section 3.3-3.4), yielding similar (±~33%) results.

Our analysis thereby establishes a quantitative link between filter-pack and real-time measurements of Mt Etna aerosol. This advances earlier work that established qualitative links between time-averaged sampling and sun-photometer observations of Chilean volcanic aerosol (Mather et al., 2004b). Quantitative analysis of SO_4^{2-}:SO_2 requires that aerosol volume and SO_2 are detected simultaneously within the same air mass, with RH and temperature also known. This was achieved here by in-situ sensor but is more challenging (and approximate) in remote sensing studies. Another condition is to reasonably constrain the aerosol volume within the measurement range. This was achieved in-situ here but seems rare in reported sun-photometer studies (Watson and Oppenheimer, 2000, 2001, Mather et al., 2004b), that may have sampled a more condensed and/or ash-rich plume. A key assumption is the $H_2SO_{4(aq)}$ or $NaHSO_{4(aq)}$ particle composition that is based on earlier chemical sampling by Martin et al. (2008). The LOAC instrument can also provide insight into particle nature (based on optical properties at two scattering angles), finding a generally absorbing signal (see Supplementary Material). This may reflect trace impurities in the sulfate aerosol that either originate from the volcanic emission or from integration of small amounts of resuspended dust. For volcanic applications elsewhere the SO_4^{2-}:SO_2 analysis method may need to be modified e.g. for metal-rich emissions where metal-acid reactions might instead lead to other compositions

e.g. Na_2SO_4, K_2SO_4, see Mather et al. (2003). For ash-rich plumes the particle volume measurement may be dominated by silica, which would obscure any estimation of sulfate. Volcanic HNO_3 contributes little to sulfate aerosol volume as it partitions largely into the gas-phase under our highly acidic plume conditions (Roberts et al., 2009). Observations of Mt Etna near-source aerosol report low ammonium content (Martin et al., 2008) with little impact on aerosol volume, however ammonia and nitrate chemistry should be considered for emissions into the boundary layer that may be more ammonia-rich.

3.3 Tracing of coincidence effects on the OPC measurement

Total aerosol volume and SO_2 are well correlated, however closer inspection of the particle number density of individual OPC size-bins shows evidence for non-linearities. Scatter plots of aerosol number with SO_2 for both Vweak and Flank data are shown in Figure 7 for three size classes. We can observe a general positive correlation, but also evidence for non-linearities: for large particle size bins, more particles are counted at higher SO_2 than expected from a linear regression. For small particle size bins, fewer particles are counted at higher SO_2 than expected from a linear regression. These trends are even more marked in the strongest crater-rim plume, where in some cases the particle number time-series anti-correlates with that of SO_2 (for raw data time-series see Supplementary Material). These non-linearities can also be seen in plots of normalized dV/dlogD as a function of particle size in Figure 8 (Flank and Vweak time-periods, where aerosol data has been normalized to a plume strength of 1 ppmv SO_2 to enable cross-comparison). In summary, the measured aerosol distribution has more large particles and fewer small particles in stronger plumes (as denoted by higher SO_2 abundance). This effect cascades across the size-distribution as a function of plume strength.

These non-linearities manifest in different ways across the size bin range. They thus cannot be attributed to uncertainties in the SO_2 measurement, also given the good agreement found between the Multi-Gas SO_2 sensors (see Supplementary Material). Below we show that LOAC OPC coincidence errors can cause similar non-linearities in the aerosol measurement at high particle concentrations. We therefore cannot attribute the observed non-linearities (solely) to natural variability or microphysical processes.

At high aerosol concentrations signals from multiple particles may be simultaneously detected by the LOAC OPC. In the case of slightly overlapping signals this causes two particles to be counted as one, whose size is classified as that of the larger particle, whilst the smaller particle is not counted, i.e. a ‘shadow effect’. Where signals overlap considerably and add together, the two observed particles may be classified as an even larger single particle. This ‘non-quantitative counting’, also known as ‘coincidence errors’ is a known OPC uncertainty; it can restrict the total number of particles counted as discussed by Renard et al. (2016) for the LOAC. Similar coincidence errors prevented a true aerosol estimate in a previous OPC deployment at Mt Etna (Vance et al., 2010). Here, the LOAC OPC measurements span plume strength over two orders of magnitude (0.3 to 30 ppmv SO_2) enabling the effect to be traced and characterised. The magnitude of the effect diminishes as plume strength decreases, and is least apparent for the Vweak dataset.

To further quantify the role of coincidence errors, a simple statistical model of the LOAC OPC is presented alongside the Vweak volumic size distribution on a linear y-axis scale (Figure 9). This model simulates how particles at a specified model input size distribution give rise to a detected signal electronically sampled at 40 kHz. The strong similarity between the "modelled measured" size distribution and the observations suggests that coincidence errors can significantly impact LOAC aerosol measurements in concentrated plumes. To further quantify the Mt Etna aerosol size distribution and derive fluxes we select optimal data at low plume strength (SO_2 = 0.3-0.4 ppmv), least affected by coincidence errors.

3.4 Quantifying Mt Etna primary aerosol size distribution and emission flux

The selected data (Vweak period at 0.3-0.4 ppmv SO_2, aerosol data normalized to 1 ppmv SO_2) are presented in Figures 10 and 11 (lognormal and linear y-axis scales, respectively) as number, area and volume distributions (where area under the d[]/dLogD vs log-scale Diameter (D) curves corresponds to total integrated number, area or volume). Measurements for each 10 s period (shown as connected data-points in blue) exhibit variation, some of which may be due to imperfect normalization using the Multi-Gas SO_2 observations. The smallest size-bin exhibits greatest data scatter (standard deviation in number = 500 cm^{-3}). The distribution shape is more easily seen by taking the mean average of each size-bin (black dots with standard error in mean). The data show a tri-modal size distribution with volume maxima around 1-2, 0.6-07 and 0.3-0.4 µm. This volumic distribution is consistent with reported time-averaged sulfate sampling (Martin et al., 2008): both exhibit maxima at supramicron particle sizes.

The measured distribution within the instrument range appears to constrain relatively well particle volume. This enables a tri-modal lognormal distribution to be fitted (black lines in Figures 10-11, see Appendix A3 for definition), whose parameters (N, D_N, σ_g for each mode) are given in **Table 5**. Our lognormal distribution fit incurs some uncertainty in the volume peak maximum between 1-2 µm (where LOAC size bin resolution is low), and in the smallest particle mode (as the smallest size-bin is subject to greatest measurement uncertainty). Nevertheless, the distribution shows distinct supra- and submicron modes, with dN/dLogD shape bearing similarity to that of Allen et al. (2006) and Shcherbakov et al. (2016).

The lognormal particle size distribution fitting facilitates comparison of different observations. This approach has been used for the fine silicate aerosol fraction at Mt Etna (Martin et al., 2008), finding a modal diameter (D_N = 0.14 µm) slightly smaller than the overall particle distribution measured in this study (D_N = 0.2-1.14 across the three modes) but with similar geometric standard deviation (σ_g = 1.3-1.45). Further comparison in terms of particle number flux is given below. Lognormal distributions were also fitted to aircraft measurements of Eyjafjallajökull plume aerosol (Schumann et al., 2011, Johnson et al., 2012). In contrast to our study the plume was aged and ash-rich. It contained fine and coarse mode particles, with overall R_{eff} = 0.1-1 µm (R_{eff} = 0.3 µm in our study; **Table 5**). The coarse-mode was of several microns diameter (volumic modal diameter D_V = 3.2-4.5), i.e. greater in size than our study and with greater geometric standard deviation (σ_g = 1.8-1.9). It showed a high silica (ash) composition. These authors also highlight deviation of the coarse aerosol distribution from the lognormal, probably due to large particle sedimentation.

Our volcanic aerosol measurement at Mt Etna made ~1.5 km downwind (with only limited time for deposition or microphysics processes) most likely reflects the primary volcanic aerosol emission. It is compared to lognormal distributions of representative atmospheric aerosols in Figure 12 (urban, rural, desert dust storm, marine, polar; Jaenicke, 1993; note actual aerosol may deviate from the representative distributions due to temporal/geographic variability). Importantly, our volcanic aerosol measurement is referenced to a plume strength of 1 ppmv SO_2. Particle numbers would be proportionally higher in stronger plume and lower in more dilute plume. At 1 ppmv SO_2 plume strength, the volcanic submicron aerosol concentration reaches similar levels to representative urban conditions, and the supra-micron aerosol concentration exceeds them. Only a desert dust storm contains more particles of micron size.

The lognormal fit parameters were used to calculate total integrated volume, area, and number (**Table 5)**. The analysis does not consider very fine nanometer-sized particles. Such particles are likely important in terms of number but are not expected to contribute significantly to volume nor surface area (Ammann and Burtscher, 1993). Aerosol/SO_2 ratios can then easily be obtained as SO_2 was co-measured (**Table 5**). Emission fluxes are estimated by combining the aerosol/SO_2 ratios with the SO_2 flux from the INGV Ultraviolet scanning spectrometer FLAME network installed at Mt Etna (Salerno et al., 2009), that reports 1800 to 2100 tonnes day SO_2 during the measurement campaign, a typical SO_2 emission flux for Mt Etna passive degassing.

Assuming a mean SO_2 flux of 1950 tonnes/day, the estimated sulfate aerosol volume flux is 5.0×10^{14} $\mu m^3\ s^{-1}$ and particle area flux 4.9×10^{15} $\mu m^2\ s^{-1}$. The number flux is 1.5×10^{16} s^{-1}, which is a lower limit that excludes numerous fine nm particles. Nevertheless, the study shows Mt Etna's sulfate particle number flux vastly exceeds the total number flux of silica particles from Mt Etna of 10^{12} s^{-1} (Martin et al., 2008). This is consistent with ash-poor quiescent degassing. The particle volume flux is converted to mass flux using an $H_2SO_{4(aq)}$ density of 1.39 g cm^{-3} (calculated for the observed 40% RH using parameterisation of Tabazadeh et al. (1997); see Appendix A1) to yield 0.7 kg s^{-1}. This contrasts by an order of magnitude with the Mt Etna sun-photometer measurements of Watson and Oppenheimer (2000) who estimated particle mass fluxes of 4.5-8 kg s^{-1} as a lower limit (assuming a water mode with density = 1 and sulfate mode with density 1.67 g cm^{-3}). One possible explanation is that two of the summit craters were exhibiting mild strombolian activity (small explosions with ash) during the field-measurements of Watson and Oppenheimer (2000), whereas our study quantifies sulfate-rich aerosol from Mt Etna during passive degassing. But it is also emphasized that volcanic sulfate aerosol is highly hygroscopic therefore volume and surface area fluxes depend strongly on relative humidity. Calculations to estimate the humidity dependence of volcanic aerosol and its role in plume chemistry are given in Section 4.

4 Discussion: role of primary volcanic aerosol on plume halogen chemistry

4.1 Aerosol hygroscopic growth as a function of humidity

Observations of hygroscopic aerosols in Mt Etna plume are most usefully interpreted in the context of the local humidity conditions. Volcanic emissions are H_2O-rich, and typically initially condensed, becoming visually transparent upon dispersion as the plume dilutes (unless ambient RH is high). The

Mt Etna emission consisted of ~80-95% H_2O with SO_2 1-5% (Roberts et al., 2017). The plume was sufficiently diluted during our field-measurements (<1 ppmv SO_2) that humidity was dominated by background RH. Here we perform calculations to estimate how the primary aerosol size distribution grows and shrinks as a function of humidity. We use the measured size distribution with fitted lognormal distribution (Figures 10-11) at known humidity (40% RH) and apply parameterisations of particle volume over a humidity range. Aerosol sulfate content was first calculated as per Section 3.2, and $H_2SO_{4(aq)}$ attributed proportionally across the (0.01 µm discretized) volumic fitted lognormal size distribution. The volume (in each 0.01 µm size-bin) was then re-calculated for a range of RH ranging from 0.1 to 99% using the $H_2SO_{4(aq)}$ molar volume parameterisation of Appendix A1. For each RH calculation, area and number were simply calculated from the new volume distributions. The calculation assumes $H_2SO_{4(aq)}$ in equilibrium with RH for planar surfaces (aerosol curvature is relevant for very small particles only and is omitted for simplicity). Similar results are also found for $NaHSO_{4(aq)}$ (not shown). Both $H_2SO_{4(aq)}$ and $NaHSO_{4(aq)}$ are highly hygroscopic, thus expected to be in the aqueous-phase (Martin et al., 2003, Tang and Munkelwitz, 1994). Ammonium sulfate can show aqueous-solid hysteresis effects but it is not expected in the near-source Mt Etna plume (nor observed: Martin et al., 2008) given high sulfate concentrations and low background ammonia. The hygroscopic aerosol growth calculation does not include HCl partitioning to aqueous-phase that can further enhance aerosol volume at very high RH (> 85%), see Martin et al. (2012) and Roberts et al. (2014b).

Figure 13a shows that particle number is conserved as the distribution shifts to higher sizes with greater RH. Aerosol surface area and volume both increase with RH, with substantial enhancements at RH > 90% (**Figure 13b,c**). The distribution remains tri-modal. However, at high RH all aerosol volumic maxima occur at supra-micron sizes (~1-10 µm), whilst at low RH there is only one volumic maximum at supramicron size (~ few µm). We suggest this RH dependency is likely a contributing factor to the different size distributions reported from Mt Etna to date (see **Tables 1-2**), noting Mather et al. (2004b) proposed condensation as an important control on particle size at volcanoes elsewhere (Villarrica, Lascar). Other sources of variability include volcanic activity (e.g. ash-poor/ash-rich) and microphysics/secondary aerosol for aged plumes.

Aerosol surface area is an important control on plume chemistry (see Section 1.2) but has been little quantified by studies to date. An estimate of the primary volcanic aerosol surface area and its RH dependency is provided in Figure 14 based on the observed aerosol and lognormal distribution at 40% RH, 285 K and the hygroscopic-growth calculations (see **Table 5** and **Figure 13b**). The primary aerosol surface area relative to SO_2 is around 2×10^{-11} μm^2 per molecule SO_2 (equivalent to 10^3 cm^2 per mole SO_2) at 40% RH. This is an order of magnitude lower than derived from reported sun-photometer measurements of near-source (1-min) plume from Villarrica volcano during Strombolian activity (Mather et al., 2004b). As mentioned above, both ash and humidity conditions affect the size distribution hence surface area.

Figure 14 predicts the humidity dependency of surface area and volume to be moderately positive below 85% RH with a very strong enhancement above 90% RH. This predicted trend is similar to $H_2SO_{4(aq)}$ growth factors e.g. as reported by Li et al. (2001). We note our study did not observe aerosol growth/water content at Mt Etna to test these calculations, nor characterise possible day-to-day/crater-to-crater variability in the primary aerosol emission. Below we apply the calculated RH

dependence of the primary aerosol surface area in a numerical model to investigate its influence on reactive halogen chemistry in the near-downwind plume.

4.2 Surface area-humidity controls on Mt Etna plume BrO, OClO chemistry

In a model sensitivity study we investigate the effect of ambient relative humidity on plume chemistry due to its predicted influence on aerosol surface area (**Figure 14**) as a control on the rate of heterogeneous reactions R1 and R2. Simulations are shown for three background atmosphere scenarios with differing ozone content as well as ambient humidities (**Figure 15**), for downwind plume evolution over 20 min. We compare the model sensitivity study to recently reported observations of Mt Etna plume chemistry: the trend in near-source plume ozone depletion quantified by Surl et al. (2015) using in-situ observations in July-August 2012 is shown as a thick yellow line. Remote sensing DOAS observations of near-downwind plume $OClO/SO_2$ alongside BrO/SO_2 made in August-September 2012 by Gliß et al. (2015) are shown as dark green data points, demonstrating an increase followed by a plateau in BrO/SO_2 as the plume travels downwind. Their observations of plume OClO build on the first discovery of OClO at Mt Etna by Bobrowski et al. (2007). $OClO/SO_2$ increases from below detection limit (light green data points) to around 3×10^{-5} mol/mol (dark green data points) over a few minutes.

The observed increase in BrO/SO_2 is well reproduced by the model although the subsequent BrO/SO_2 plateau is slightly overestimated towards the end of the simulation. Near-downwind plume ozone depletion is also well reproduced, with the model predicting a partial recovery further downwind. The box model also succeeds in simulating $OClO/SO_2$ in broad agreement with that observed (within an order of magnitude), with $OClO/SO_2$ increasing to a maximum several minutes downwind. This modelling capability for reactive chlorine had not been demonstrated previously.

The model predicts that relative humidity enhances BrO in the downwind plume, but has a rather small influence on BrO near to source. This is initially surprising given the well-known importance of volcanic aerosol surface area in catalysing the formation of BrO (Bobrowski et al., 2007, Roberts et al., 2009, Von Glasow, 2010). A model explanation is provided, based on the predicted Br-speciation of Roberts et al. (2014a): whilst reactive bromine formation is strongly aerosol-dependent, the near-downwind BrO/SO_2 is instead largely controlled by aerosol-independent cycling between Br and BrO (reactions R4 and R7). This mechanism may provide an explanation for the lack of correlation between ambient RH and BrO/SO_2 in Mt Etna plume at 6 km downwind reported by Bobrowski and Guiffrida (2012). Further downwind, BrO/SO_2 is controlled by partitioning between HOBr, $BrONO_2$ and BrO (reactions R1-R6), whose interconversion does depend on aerosol. Hence higher RH promotes BrO/SO_2 far downwind. A greater rate of ozone depletion is also predicted at higher RH, as the enhanced surface area yields a higher rate of reactive bromine cycling. Figure 15 shows that near-downwind $OClO/SO_2$ is enhanced at higher RH. This reflects the role of aerosol in the conversion of volcanic HBr into reactive halogens: a faster depletion of HBr (and $Br^-_{(aq)}$) at high RH promotes formation of BrCl from reaction R2. Reactive chlorine formation is thus greater at higher surface area or RH. An interesting model finding is the influence of background atmospheric composition on plume OClO. Plumes dispersing into a more polluted O_3-rich troposphere produce more OClO. The model explanation is that OClO production requires formation of ClO (alongside

BrO), which is produced from reaction of Cl with ozone in competition with loss of Cl, e.g. by reaction with CH_4. The plume reactive halogen chemistry itself depletes ozone, nevertheless a more O_3-rich background atmosphere will yield higher absolute in-plume ozone concentrations and hence more OClO.

Further insights are gained from the spatially resolved model simulations (**Figure 16 and 17**). The halogen cycling is most rapid in the plume centre, where Br and BrO absolute concentrations are the highest, causing greatest ozone loss. As consequence reactive bromine partitions to Br and the BrO/SO_2 ratio is diminished in the plume centre compared to the plume edge. OClO is also slightly enhanced at the plume edge, the region where BrO and plume ozone (required to form ClO from Cl) are more abundant. This pattern concurs with reported measured spatial trends in BrO/SO_2 and $OClO/SO_2$ (Bobrowski et al., 2007, General et al., 2015, Gliss et al., 2015). Simulations with higher bromine emission (**Figure 17**) show greater BrO/SO_2 and ozone depletion but a delayed rise in $OClO/SO_2$. This is due to the delayed depletion of HBr thus later onset of BrCl formation, as well as to the lower in-plume ozone.

Overall, the model shows a good general capability to reproduce these Mt Etna plume observations although it is emphasized that the model parameter space is vast. Several aspects of the emission-plume are only partially constrained and may vary with volcanic or meteorological conditions. These include the high-temperature emission-initialisation, extents of plume-air mixing, and bromine-NO_x chemical coupling, as discussed by Roberts et al. (2014a) and Surl et al. (2015). Our measurement of the primary volcanic aerosol emission (and its surface area) informs one important aspect of this complex parameter space (but we did not investigate particle processing/secondary aerosol which will become increasingly important as the plume disperses downwind). Besides aerosol observations, measurements of additional reactive halogen species beyond BrO and OClO are needed to help better constrain volcanic plume chemistry models.

4. Conclusions

Volcanoes are an important source of aerosols to the troposphere impacting atmospheric chemistry and possibly climate evolution. Reactions on the aerosol surface area catalyse the conversion of co-emitted volcanic halogens (HBr, HCl) into reactive forms (BrO, OClO) that deplete ozone. The primary volcanic aerosol emission is an important driver of this process but has been only partially quantified by studies to date of quiescently degassing (ash-poor) volcano plumes. This presents a limitation to initialising models of volcano plume atmospheric impacts. We present a high-resolution (0.1 Hz) real-time in-situ study at Mt Etna during passive degassing that co-deployed a LOAC optical particle counter (with 19 size-bins over 0.2-50 µm in diameter) to characterise the aerosol number and size-distribution alongside Multi-Gas SO_2 sensors, **Figures 3-5**. The in-situ aerosol/SO_2 is combined with remote sensing SO_2 flux to yield aerosol emission flux. Our data analysis focuses on near-downwind (~1.5 km) grounding volcanic plume, having traced OPC coincidence errors in the more concentrated plume measured nearer-to-source that affect the aerosol size distribution retrieval (**Figures 7 – 9**).

Total particle volume correlated strongly with SO_2 (as a plume tracer), **Figure 6**. Further analysis is performed assuming the volcanic aerosol volume is dominated by $H_2SO_{4(aq)}$ or $NaHSO_{4(aq)}$: by analysing the co-measured volcanic aerosol and SO_2 we derive SO_4^{2-}/SO_2 ratios of 1-2 % that are

consistent with values reported from filter-pack aerosol sampling, **Table 4**. A multi-modal volcanic aerosol size distribution is identified at 40% RH, with volume median diameters 1-2, 0.6-07 and 0.3-0.4 μm, **Figures 10-11, Table 5**. Episodes of re-suspended dust were also observed that generated larger particles. Lognormal fits to the observed volcanic particle size distribution provide parameters for initialisation of atmospheric models and enable the primary aerosol emission from Mt Etna to be compared to other reported distributions. At 1 ppmv SO_2 plume strength, the volcanic submicron aerosol concentration reaches similar levels to representative urban conditions, and the supra-micron aerosol concentration exceeds them, **Figure 12**.

Hygroscopic calculations predict that total surface area of the primary aerosol emission becomes strongly enhanced at high relative humidity, **Figure 13-14**. A numerical model of the plume atmospheric chemistry is used to evaluate the role of primary aerosol surface area and its humidity dependence on volcanic plume BrO and OClO chemistry, **Figures 15-17**. On near-downwind (a few km) scales BrO/SO_2 is simulated to have little dependence on ambient RH. This surprising finding - that can be explained by the model chemistry - is of value to interpreting volcanic BrO monitoring data. Aerosol and RH exert stronger controls on OClO and on BrO further downwind. Alongside BrO formation and ozone depletion, OClO formation is simulated in broad quantitative agreement with recent Mt Etna observations. $OClO/SO_2$ reaches a maximum a few minutes downwind. High background ozone is shown to promote OClO formation whilst a high volcanic HBr emission delays the rise in $OClO/SO_2$. The model plume chemistry predicts strong spatial variations between plume edge and centre demonstrating the role of plume-air mixing.

This study focuses on the size distribution of primary aerosol from passively degassing Mt Etna volcano, measured just 1.5 km, ~2 min from the crater. Using the same LOAC instrumentation operated on a balloon we have very recently also reported aerosol size distributions in relatively young tropospheric plume (8 km, ~15 min) downwind from the Icelandic Holuhraun effusive eruption (Vignelles et al., 2016). Interestingly, both studies show evidence for supra- and sub-micron modes with the sub-micron mode relatively more enhanced for the more aged plume case. This might reflect an expected consequence of in-plume atmospheric oxidation of SO_2. However, we emphasize that in each case the primary aerosol emission likely depends on many factors (near-vent mixing, temperature, magmatic composition, etc.) that are specific to the volcanic source.

Acknowledgements

This study was financed by LABEX VOLTAIRE (VOLatils-Terre Atmosphère Interactions – Ressources et Environnement) ANR-10-LABX-100-01 (2011–20). We are grateful to Alphasense Ltd for sensor advice and thank M Tagger and B. Scaillet for initiating this project. We thank J. Gliβ and N. Bobrowski for providing plume observation data from Gliβ et al. (2015), and for useful discussions. TJR acknowledges The Aerosol Society and Darwin College, who supported her attendance of the "Halogens in Volcanic Systems" workshop that informed this project's research goals. AA acknowledges funding from the European Research Council under the European Union's Seventh Framework Programme (FP7/2007/2013)/ERC grant agreement nr 305377. We thank A. Amantia, M. Cantarero and G. Spata for fieldwork assistance and T. Caltabiano for assistance in gas flux data processing. This study contributes to ChArMEx (the Chemistry-Aerosol Mediterranean Experiment)

WP1 on atmospheric emissions in the Mediterranean region, as well as ANR-STRAP (Trans-disciplinary collaboration to investigate volcano plumes risks).

References

Allen A. G., Mather T. A., McGonigle A. J. S., Aiuppa A., Delmelle P., Davison B., Bobrowski N., Oppenheimer C., Pyle D. M. and Inguaggiato S. (2006) Sources, size distribution and downwind grounding of aerosols from Mt Etna. *J. Geophys. Res.* **111**, D10302**,** doi: 10.1029/2005JD006015.

Ammann M. and Burtscher H. (1993) Aerosol dynamics and light-scattering properties of a volcanic plume. *J. Geophys. Res.* **98**, 19705-19711.

Ammann M., Hauert R., Burtscher H. and Siegmann H. C. (1993) Photoelectric charging of ultrafine volcanic aerosols: Detection of Cu(I) as a tracer of chlorides in magmatic gases. *J. Geophys. Res.* **98**, 551-556.

Bobrowski N. Von Glasow R., Aiuppa A., Inguaggiato S., Louban I., Ibrahim O. W. and Platt U. (2007) Reactive halogen chemistry in volcanic plumes. *J. Geophys. Res.: Atmos.* **112**, D6, D06311, doi:10.1029/2006JD007206.

Bobrowski N. and Guiffrida G. (2012) Bromine monoxide / sulphur dioxide ratios in relation to volcanological observations at Mt. Etna 2006–2009. *Solid Earth* **3**, 433–445, doi:10.5194/se-3-433-20122012.

Buck A. L. (1981) New equations for computing vapor pressure and enhancement factor. J. *Appl. Meteorol.* **20**, 1527–1532.

Bussinger S., Huff R., Pattantyus A., Horton K., Sutton A. J., Elias T. and Cherubini T. (2015) Observing and Forecasting Vog Dispersion from Kīlauea Volcano, Hawaii. *Bull. Am. Meteor. Soc.* **96**, 10, 1667-1686.

Carn S. A., Froyd K. D., Anderson B. E., Wennberg P., Crounse J., Spencer K., Dibb J. E., Krotkov N. A., Browell E. V., Hair J. W. and Diskin G. (2011) In situ measurements of tropospheric volcanic plumes in Ecuador and Colombia during TC4. *J. Geophys. Res.: Atmos.* **116**, D10.

Davidson G. A. (1990) A modified power law representation of the Pasquill-Gifford dispersion coefficients, J. Air Waste Manage. Assoc. 40,1146-1147.

Donovan A, Tsanev V, Oppenheimer C, Edmonds M. (2014) Reactive halogens (BrO and OClO) detected in the plume of Soufrière Hills Volcano during an eruption hiatus. *Geochem. Geophys. Geosyst.* **15**, 3346-3363.

Ebmeier S. K., Sayer A. M., Grainger R. G., Mather T. A. and Carboni, E. (2014) Systematic satellite observations of the impact of aerosols from passive volcanic degassing on local cloud properties. *Atmos. Chem. Phys.* **14**, 10601-10618, doi:10.5194/acp-14-10601-2014.

General S., Bobrowski N., Pöhler D., Weber K., Fischer C. and Platt U. (2015) Airborne I-DOAS measurements at Mt. Etna: BrO and OClO evolution in the plume. *J. Volcanol. Geotherm. Res.* **300**, 175-186.

Gliß J., Bobrowski N., Vogel L., Pöhler D. and Platt U. (2015). OClO and BrO observations in the volcanic plume of Mt. Etna–implications on the chemistry of chlorine and bromine species in volcanic plumes. *Atmos. Chem. Phys.* **15**, 5659-5681.

Halmer M. M., Schmincke H.-U., and Graf H.-F. (2002) The annual volcanic gas input into the atmosphere, in particular into the stratosphere: a global data set for the past 100 years. *J. Volcanol. Geotherm. Res.* **115**, 511-528.

Ilyinskaya E., Oppenheimer C., Mather T. A., Martin R. S. and Kyle P. R. (2010) Size-resolved chemical composition of aerosol emitted by Erebus volcano, Antarctica. *Geochem. Geophys. Geosyst.* **11**, Q03017, doi:*10.1029/2009GC002855*.

Jaenicke R. (1993) Tropospheric aerosols. In Aerosol-Cloud-Climate Interactions (Ed. P. V. Hobbs), Academic Press, 1-31.

Johnson B., Turnbull K., Brown P., Burgess R., Dorsey J. Baran A. J., Webster H., Haywood J., Cotton R., Ulanowski Z., Hesse E., Woolley A. and Rosenberg P. (2012) In situ observations of volcanic ash clouds from the FAAM aircraft during the eruption of Eyjafjallajökull in 2010. *J. Geophys. Res.* **117**, D00U24, doi:10.1029/2011JD016760.

Jourdain L., Roberts T. J., Pirre M. and Josse B. (2016) Modeling the reactive halogen plume from Ambrym volcano and its impact on the troposphere with the CCATT-BRAMS mesoscale model. *Atmos. Chem. Phys.* **16**, 12099-12125.

Kelly P. J., Kern C., Roberts T. J., Lopez T., Werner C. and Aiuppa A. (2013) Rapid chemical evolution of tropospheric volcanic emissions from Redoubt Volcano, Alaska, based on observations of ozone and halogen-containing gases. *J. Volcanol. Geotherm. Res.* **259**, 317-333.

Kroll J. H., Cross E. S., Hunter J. F., Pai S., Wallace L. M., Croteau P. L., Jayne J. T., Worsnop D. R., Heald C. L., Murphy J. G., and Frankel S. L. (2015) Atmospheric evolution of sulfur emissions from Kılauea: real-time measurements of oxidation, dilution, and neutralization within a volcanic plume. Environmental Science & Technology, **49**, **7**, 4129-37.

Li J., Wong J. G., Dobbie J. S. and Chýlek P. (2001) Parameterization of the optical properties of sulfate aerosols. *J. Atmos. Sci.* **58**, 193-209.

Lurton T., Renard J.-B., Vignelles D., Jeannot M., Akiki R., Mineau J.-L. and Tonnelier T. (2014) Light scattering at small angles by atmospheric irregular particles: modelling and laboratory measurements. *Atmos. Meas. Tech.* **7**, 931-939, doi:10.5194/amt-7-931-2014.

Martin, S.T., Schlenker, J.C., Malinowski, A., Hung, H.M. and Rudich, Y. (2003) Crystallization of atmospheric sulfate-nitrate-ammonium particles. Geophysical research letters, **30**, **21**, 2102, doi:10.1029/2003GL017930.

Martin R. S., Mather T. A. and Pyle D. M. (2006) High-temperature mixtures of magmatic and atmospheric gases. *Geochem. Geophys. Geosyst.* **7**, Q04006, doi:10.1029/2005GC001186.

Martin R. S., Mather T. A., Pyle D. M., Power M., Allen A. G., Aiuppa A., Horwell C. J. and Ward E. P. W. (2008) Composition-resolved size distributions of volcanic aerosols in the Mt. Etna plumes. *J. Geophys. Res.* **113**, D17211, doi:10.1029/2007JD009648.

Martin R. S., Roberts T. J., Mather T. A. and Pyle D. M. (2009) The implications of H 2 S and H 2 kinetic stability in high-T mixtures of magmatic and atmospheric gases for the production of oxidized trace species (eg, BrO and NO_x). *Chem. Geol.* **263**, 143-150.

Martin R. S., Wheeler J. C., Ilyinskaya E., Braban C. F. and Oppenheimer C. (2012) The uptake of halogen (HF, HCl, HBr and HI) and nitric (HNO_3) acids into acidic sulfate particles in quiescent volcanic plumes. *Chem. Geol.* **296**, 19-25.

Martin R. S., Ilyinskaya E. and Oppenheimer C. (2012) The enigma of reactive nitrogen in volcanic emissions. *Geochim. Cosmochim. Acta* **95**, 93-105.

Mather T. A., Allen A. G., Oppenheimer C., Pyle D. and McGonigle A. J. S (2003) Size-resolved characterisation of soluble ions in the particles in the tropospheric plume of Masaya Volcano, Nicaragua: Origins and plume processing. *J. Atmos. Chem.* **46**, 207–237.

Mather T. A., Pyle D. M. and Oppenheimer C. (2004a) Tropospheric volcanic aerosol.In Volcanism and the Earth's Atmosphere (Eds. A. Robock and C. Oppenheimer), American Geophysical Union Monograph Series **139**, 189-212.

Mather T. A., Tsanev V. I., Pyle D. M., McGonigle A. J. S., Oppenheimer C. and Allen A. G. (2004b) Characterization and evolution of tropospheric plumes from Lascar and Villarrica volcanoes, Chile. *J. Geophys. Res.*, **109**, D21303.

Mather T. A., McCabe J. R., Rai V. K., Thiemens M. H., Pyle D. M., Heaton T. H. E., Sloane H. J. and Fern G. R. (2006) Oxygen and sulfur isotopic composition of volcanic sulfate aerosol at the point of emission. *J. Geophys. Res.* **111**, D18205**.**

Oppenheimer C., Kyle P., Eisele F., Crawford J., Huey G., Tanner D., Saewung K., Mauldin L., Blake D., Beyersdorf A., Buhr M. and Davis D. (2010), Atmospheric chemistry of an Antarctic volcanic plume. *J. Geophys. Res.* **115**, D04303, doi:10.1029/2009JD011910.

Quisefit JP, Bergametti G, Tedesco D, Pinart J, and Colin JL (1988) Origin of particulate potassium in Mt Etna emissions before and during the 1983 eruption. *J. Volcanol. Geotherm. Res.* **35**, 111-119.

Platt U. and Stutz J (2008) *Differential Optical Absorption Spectroscopy: Principles and Applications*. Springer-Verlag, Heidelberg, 272 pp.

Renard J.-B., Dulac F., Berthet G., Lurton T., Vignelles D., Jégou F., Tonnelier T., Thaury C., Jeannot M., Couté B., Akiki R., Mineau J.-L., Verdier N., Mallet M., Gensdarmes F., Charpentier P., Mesmin S., Duverger V., Dupont J.-C., Elias T., Crenn V., Sciare J., Giacomoni J., Gobbi M., Hamonou E., Olafsson H., Dagsson-Waldhauserova P., Camy-Peyret C., Mazel C., Décamps T.,

Piringer M., Surcin J. and Daugeron D. (2016) LOAC: a small aerosol optical counter/sizer for ground-based and balloon measurements of the size distribution and nature of atmospheric particles – Part 1: Principle of measurements and instrument evaluation. *Atmos. Meas. Tech.* **9**, 1721-1742, doi:10.5194/amt-9-1721-2016.

Roberts T. J, Braban., C. F., Martin R. S., Oppenheimer C., Adams J. W., Cox R. A., Jones R. L. and Griffiths P. T. (2009) Modelling reactive halogen formation and ozone depletion in volcanic plumes. *Chem. Geol.* **263**, 1, 151-163.

Roberts T. J., Braban C., Oppenheimer C., Martin R. S., Saffell J. R., Dawson D., Freshwater R. A., Griffiths, P. T. and Jones R. L. (2012) Electrochemical sensing of volcanic plumes. *Chem. Geol.* **332-333**, 74–91.

Roberts T. J., Martin R. S. and Jourdain L. (2014a) Reactive halogen chemistry in Mt Etna's volcanic plume: the influence of total Br, high temperature processing, aerosol loading and plume-air mixing (volcanic emissions flux). Atmos. Chem. Phys. **14**, 11201–11219, doi:10.5194/acp-14-11201-2014.

Roberts T. J., Jourdain L. Griffiths P. T. and Pirre M. (2014b) Re-evaluating the reactive uptake of HOBr in the troposphere with implications for the marine boundary layer and volcanic plumes. Atmos. Chem. Phys. **14**, 11185-11199, doi:10.5194/acp-14-11185-2014.

Roberts T. J., Lurton T., Giudice G., Liuzzo M., Aiuppa A., Coltelli M., Vignelles D., Salerno G., Couté B., Chartier M., Baron R., Saffell J. R. and Scaillet B. (2017) Validation of a novel multi-gas sensor for volcanic HCl alongside H_2S and SO_2 at Mt Etna. *Bull. Volcanol.*, **79**, **36**, doi:10.1007/s00445-017-1114-z.

Salerno G. G., Burton M., Oppenheimer C., Caltabiano T., Randazzo D. and Bruno N. (2009) Three-years of SO_2 flux measurements of Mt. Etna using an automated UV scanner array: comparison with conventional traverses and uncertainties in flux retrieval. *J. Volcanol. Geotherm. Res.* **183**, 76-83, doi:10/1016j.jvolgeores.2009.02.013.

Schmidt A., Carslaw K. S., Mann G. W., Rap A., Pringle K. J., Spracklen D. V., Wilson M. and Forster P. M. (2012) Importance of tropospheric volcanic aerosol for indirect radiative forcing of climate. *Atmos. Chem. Phys.* **12**, 7321-7339.

Schumann U., Weinzierl B., Reitebuch O., Schlager H., Miniki A., Forster C., Baumann R., Saile T., Graf K., Mannstein H., Voigt C., Rahm S., Simmet R., Scheibe M., Lichtenstern M., Stock P., Rüba H., Schäuble D., Tafferner A., Rautenhaus M., Gerz T., Ziereis H., Krautstrunk M., Mallaun C., Gayet J.-F., Lieke. K., Kandler K., Ebert M., Weinbruch S., Stohl A., Gasteiger J., Groß S., Freudenthaler V., Wiegner M., Ansmann A., Tesche M., Olafsson H. and Sturm K. (2011) Airborne observations of the Eyjafjalla volcano ash cloud over Europe during air space closure in April and May 2010. *Atmos. Chem. Phys.* **11**, 2245–2279.

Scollo S., Kahn R. A., Nelson D. L., Coltelli M., Diner D. J., Garay M. J. and Realmuto V. J. (2012) MISR observations of Etna volcanic plumes. *J. Geophys. Res.* **117**, D06210, doi: doi:10.1029/2011JD016625.

Seinfeld J. H. and Pandis S. N. (2006) Atmospheric Chemistry and Physics. John Wiley & Sons, Chapter 7.

Sellitto P., di Sarra A., Corradini S., Boichu M., Herbin H., Dubuisson P., Sèze G., Meloni D., Monteleone F., Merucci L., Rusalem, J., Salerno G., Briole P. and Legras B. (2016) Synergistic use of Lagrangian dispersion modelling, satellite and surface remote sensing measurements for the investigation of volcanic plumes: the Mount Etna eruption of 25–27 October 2013. *Atmos. Chem. Phys.* **16**, 6841-6861.

Shcherbakov V., Jourdan O., Voigt C., Gayet J.-F., Chauvigne A., Schwarzenboeck A., Minikin A., Klingebiel M., Weigel R., Borrmann S., Jurkat T., Kaufmann S., Schlage R., Gourbeyre C., Febvre G., Lapyonok T., Frey W., Molleker S. and Weinzierl B. (2016) Porous aerosol in degassing plumes of Mt. Etna and Mt. Stromboli. *Atmos. Chem. Phys.* **16**, 11883-11897, doi:10.5194/acp-16-11883-2016, 2016.

Shinohara H., Aiuppa A., Giudice G., Gurrieri S., and Liuzzo M. (2008) Variation of H_2O/CO_2 and CO_2/SO_2 ratios of volcanic gases discharged by continuous degassing of Mount Etna volcano, Italy. *J. Geophys. Res.* **113**, B09203, doi:10.1029/2007JB005185.

Spinetti C. and Buongiorno M. F. (2007) Volcanic aerosol optical characteristics of Mt. Etna tropospheric plume retrieved by means of airborne multispectral images. J. Atmos. Solar-Terr. Phys. **69**, 981-994.

Surl L., Donohoue D., Aiuppa A., Bobrowski N. and von Glasow R. (2015) Quantification of the depletion of ozone in the plume of Mount Etna. *Atmos. Chem. Phys.* **15**, 2613-2628, doi:10.5194/acp-15-2613-2015.

Tabazadeh A., Toon O. B., Clegg S. L. and Hamill P. (1997) A new parameterization of H_2SO_4/H_2O aerosol composition: atmospheric implications. *Geophys. Res. Lett.* **24**, 1931-1934.

Tang I. N. and Munkelwitz H. R. (1994) Water activities, densities, and refractive indices of aqueous sulfates and sodium nitrate droplets of atmospheric importance. *J. Geophys. Res. Atmos.* **99**, 18801-18808.

Theys N., De Smedt I., Van Roozendael M., Froidevaux L., Clarisse L. and Hendrick F. (2014) First satellite detection of volcanic OClO after the eruption of Puyehue-Cordón Caulle. *Geophys. Res. Lett.* **41**, 667-672.

Toutain J.-P., Quisefit J.-P., Briole P., Aloupogiannis P., Blanc P. and Robaye G. (1995) Mineralogy and chemistry of solid aerosols emitted from Mount Etna. *Geochem. J.* **29**, 163-173.

Vance A., McGonigle A. J. S., Aiuppa A., Stith J. L. Turnbull K. and von Glasow R. (2010) Ozone depletion in tropospheric volcanic plumes. *Geophys. Res. Lett.* **37**, L22802, doi:10.1029/2010GL044997.

Vignelles D., Roberts T.J., Carboni E., Ilyinskaya E., Pfeffer M., Dagsson-Waldhauserova P., Schmidt A., Berthet G., Jegou F., Renard J.-B., Ólafsson H., Bergsson B., Yeo R., Fannar Reynisson N., Grainger R.G., Galle B., Conde V., Arellano S., Lurton T., Couté B. and Duverger V. (2016)

Balloon-borne measurement of the aerosol size distribution from an Icelandic flood basalt eruption. *Earth Planet. Sci. Lett.* **453**, 252–259.

Vié le Sage R. (1983) Chemistry of the volcanic aerosol. In Forecasting Volcanic Events (Ed. H. Tazieff and J-C Sabroux), Elsevier, Amsterdam, 445-474.

von Glasow R., Bobrowski N. and Kern C. (2009) The effects of volcanic eruptions on atmospheric chemistry. Chem. Geol. **263**, 131-42.

von Glasow R. (2010) Atmospheric chemistry in volcanic plumes. Proc. Nat. Acad. Sci. **107**, 6594-6599.

Watson I. M. and Oppenheimer C. (2000) Particle size distributions of Mount Etna's aerosol plume constrained by Sun photometry. *J. Geophys. Res.*, **105**, 9823-9829.

Watson I. M. and Oppenheimer C. (2001) Photometric observations of Mt. Etna's different aerosol plumes., *Atmos. Environ.* **35**, 3561-3572.

Witt M. L. I., Mather T. A., Pyle D. M., Aiuppa A., Bagnato E. and Tsanev V. I. (2008) Mercury and halogen emissions from Masaya and Telica volcanoes, Nicaragua. *J. Geophys. Res.* **133**, B06203, doi:10.1029/2007JB005401.

Wittmer, J., Bobrowski N., Liotta M., Giuffrida, G., Calabrese S. and Platt U. (2014) Active alkaline traps to determine acidic-gas ratios in volcanic plumes: Sampling techniques and analytical methods. *Geochem. Geophys. Geosyst.* **15**, 2797–2820, doi:10.1002/2013GC005133.

Figures

Figure 1. Schematic showing role of aerosol in volcanic plume halogen chemistry that converts emitted HBr and HCl into reactive halogens BrO and OClO. Chemical cycles at ambient temperature are 'kick-started' by the high-temperature production of radicals and sulfate aerosol precursors.

Figure 2. Map of Etna volcano summit, showing the measurement track that sampled the three summit crater emissions before descending on the flank, as well as the location of near-downwind grounding plume (~1.5 km from summit) sampled on 02 and 04 October, 2012.

Figure 3. (a) Time-series of SO_2 mixing ratio and (b) total aerosol volume density measured by Multi-Gas and LOAC OPC on 02 October 2012.

Figure 4. Selected 'Vweak' time-period: (a) time-series of SO_2 mixing ratio and (b) total aerosol volume density measured by Multi-Gas and LOAC OPC. See Figure 3 for Multi-Gas sensor legend.

Figure 5. Selected 'DW1' and 'DW2' time-period: (a) time-series of SO_2 mixing ratio and (b) total aerosol volume density measured by Multi-Gas and LOAC OPC. See Figure 3 for Multi-Gas sensor legend.

Figure 6. Scatter plot of total aerosol volume density and SO_2 mixing ratio during four selected time-periods (Vweak, Flank, DW1, DW2), measured at 0.1 Hz by LOAC OPC and Multi-Gas, respectively. Also shown is the linear regression on 'Vweak' dataset, that has gradient 64.8 $\mu m^3\ cm^{-3}$ per ppmv SO_2 and intercept 2.2 $\mu m^3\ cm^{-3}$.

Figure 7. Particle number density versus SO_2 mixing ratio shown for three aerosol size-bins: 3-5, 1-3 and 0.9-1.1 µm diameter (upper, middle, lower, respectively). Both 'Vweak' and 'Flank' datasets are shown in each panel.

Figure 8. Volumic aerosol size distribution for the (a) 'Flank' and (b) 'Vweak' datasets. Aerosol dV/dLogD data has been normalized for 1 ppmv SO_2 and is coloured according to plume strength denoted by co-measured SO_2.

Figure 9. a: volumic aerosol size distribution for the 'Vweak' dataset where aerosol dV/dLogD data has been normalized for 1 ppmv SO_2 and is coloured according to plume strength denoted by co-measured SO_2. b: instrument model predicts a 'measured' size distribution for a given input distribution. Both plots exhibit enhancements in the 1-2 µm range.

Figure 10. Aerosol size distribution for selected data (when SO_2 = 0.3-0.4 ppmv) from the Vweak time-period, shown as (a) number, (b) surface area and (c) volumic distributions. The d[]/dLogD datasets have been normalized to 1 ppmv SO_2 and are shown with logarithmic y-axis. Each 10 s size distribution measurement is shown (blue lines, connecting the simultaneous observations in each size-bin) as well as time-averaged mean values for each size-bin (black dots) with standard error in the mean. The fitted multi-modal lognormal distribution exhibits peaks corresponding to three modes.

Figure 11. Aerosol size distributions for selected data (when SO_2 = 0.3-0.4 ppmv) from the Vweak time-period, shown as (a) number, (b) surface area and (c) volumic distributions. The d[]/dLogD

datasets have been normalized to 1 ppmv SO_2 and are shown with linear y-axis. Each 10 s size distribution measurement is shown (blue lines, connecting the simultaneous observations in each size-bin) as well as time-averaged mean values for each size-bin (black dots) with standard error in the mean. The fitted multi-modal lognormal distribution exhibits peaks corresponding to three modes.

Figure 12. Primary volcanic aerosol from Mt Etna from this work shown alongside representative atmospheric aerosols (urban, rural, desert dust storm, marine, polar) from Jaenicke (1993). The lognormal distributions are shown as dN/dLog10(R) versus Radius. The volcanic aerosol distribution shown is for primary aerosol at a plume of strength 1 ppmv SO_2 on Mt Etna flank. See **Table 5** for details. Note that our volcanic particle size distribution misses the fraction <0.1 µm due to instrumental limitations.

Figure 13. Aerosol size distributions calculated across a range of relative humidity, based on the selected data of Figures 9 and 10 and a hygroscopic aerosol growth model (see Section 3.5 and Appendix A3 for details). The size distributions are shown as (a) number, (b) surface area and (c) volumic distributions.

Figure 14. (a) Total surface area and (b) total volume (per ppmv SO_2 or per mole sulfate) calculated across a range of relative humidity, based on the selected data of Figures 9 and 10 and a hygroscopic aerosol growth model. The underlying distributions are presented in Figure 12.

Figure 15. Simulated downwind plume chemical evolution according to the *PlumeChem* model. (a) BrO, (b) OClO and (c) ozone loss are predicted relative to SO_2 as a plume tracer, and compared to reported observations. The trend in ozone depletion observed by in-situ measurelents of Surl et al. (2015) is shown as a thick yellow line. Observations of BrO/SO_2 and $OClO/SO_2$ by Gliß et al. (2015) are shown in dark green (with low $OClO/SO_2$ near-to-source confirmed by measurements below the detection limit shown in light green). Model runs are presented for 10, 50 and 90 % ambient relative humidity, and at background ozone mixing ratios of 30, 60 and 100 ppbv.Figure 16. Plume (a) SO_2, (b) BrO/SO_2, (c) ozone depletion and (d) $OClO/SO_2$ simulated downwind and across-plume by the *PlumeChem* model assuming molar $HBr/SO_2 = 4.8\ 10^{-4}$.

Figure 17. Plume (a) SO_2, (b) BrO/SO_2, (c) ozone depletion, and (d) $OClO/SO_2$ simulated downwind and across-plume by the *PlumeChem* model assuming molar $HBr/SO_2 = 7.4\times10^{-4}$. Note change in scale for BrO/SO_2 compared to Figure 16.

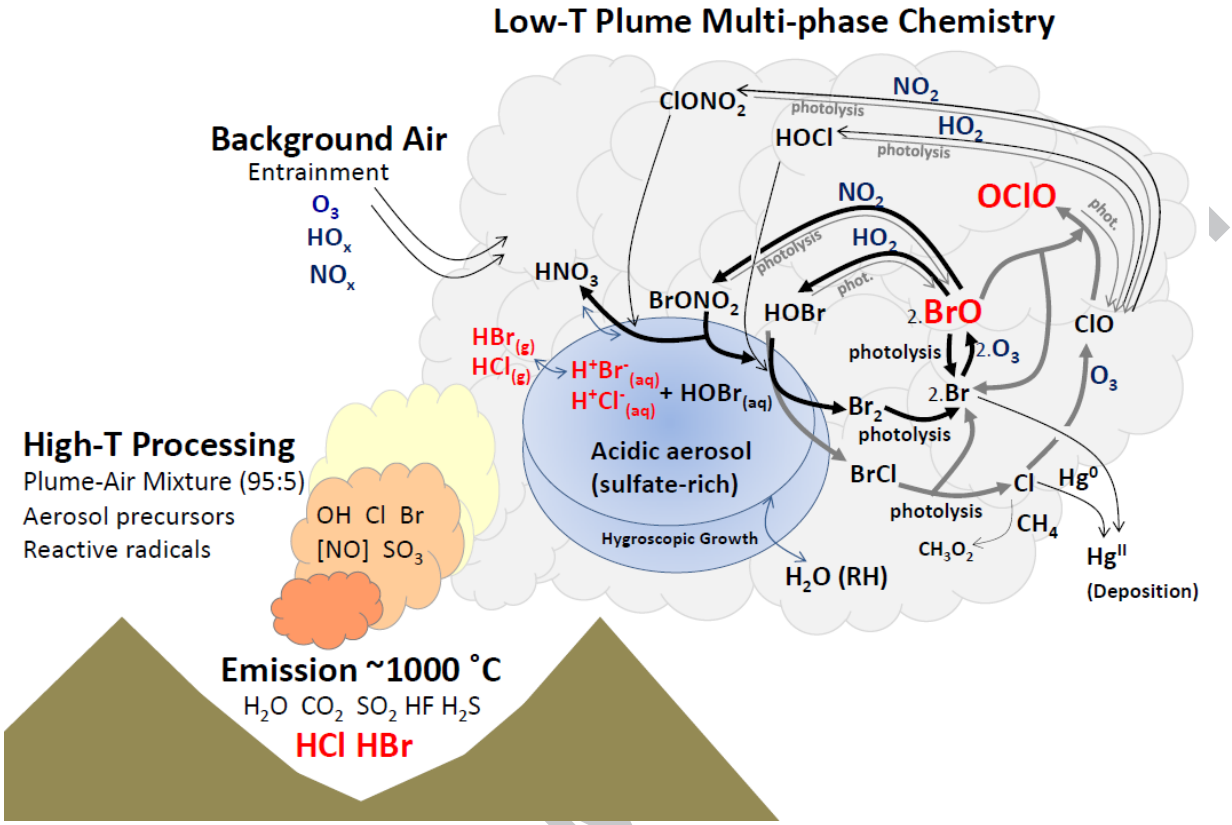

Figure 1

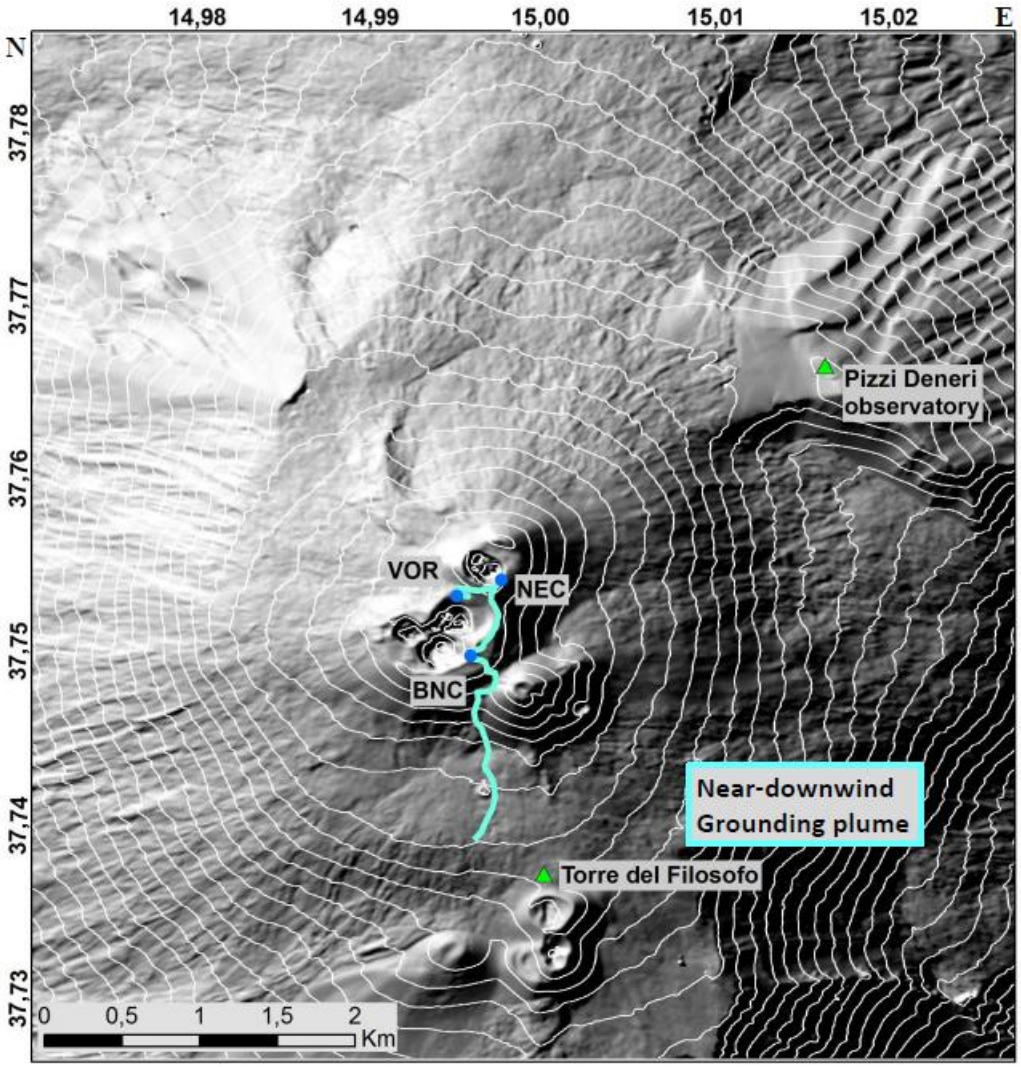

Figure 2

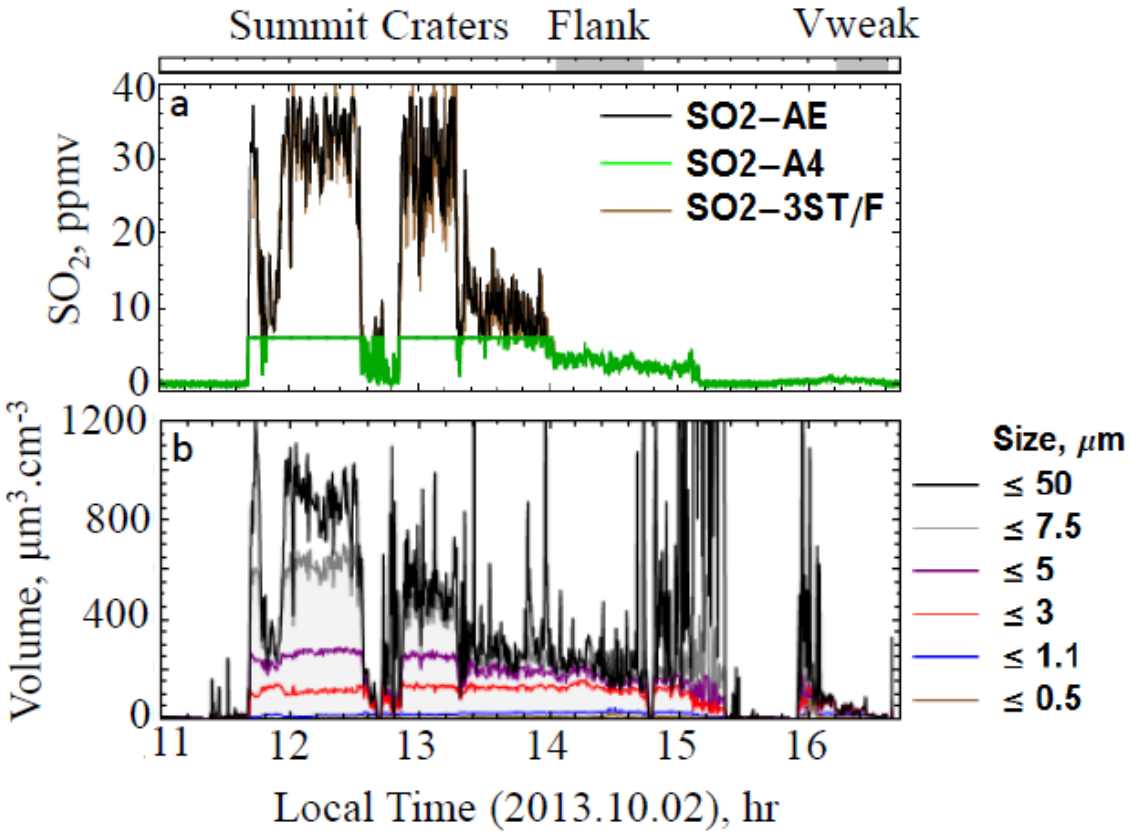

Figure 3

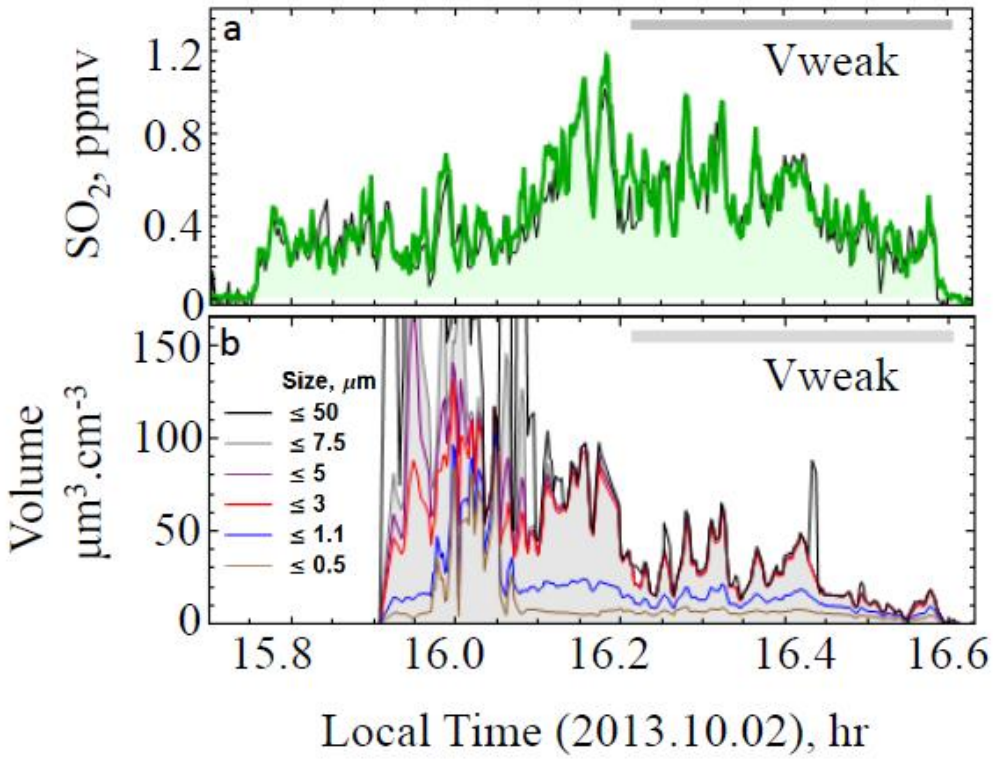

Figure 4

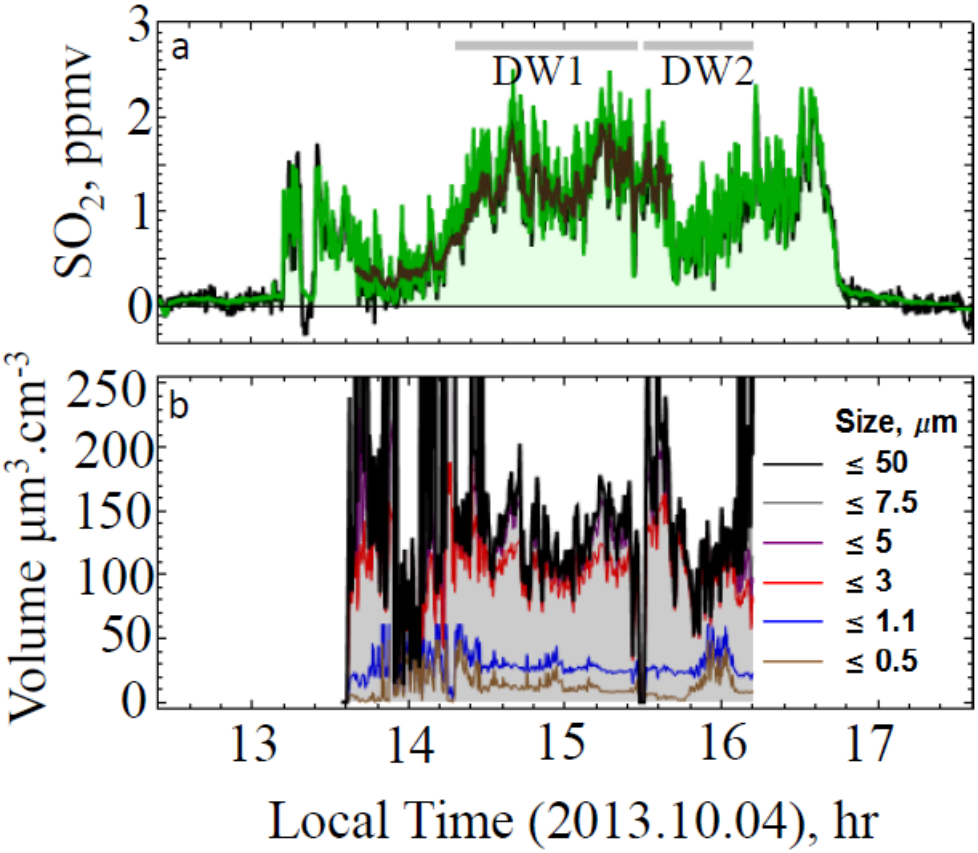

Figure 5

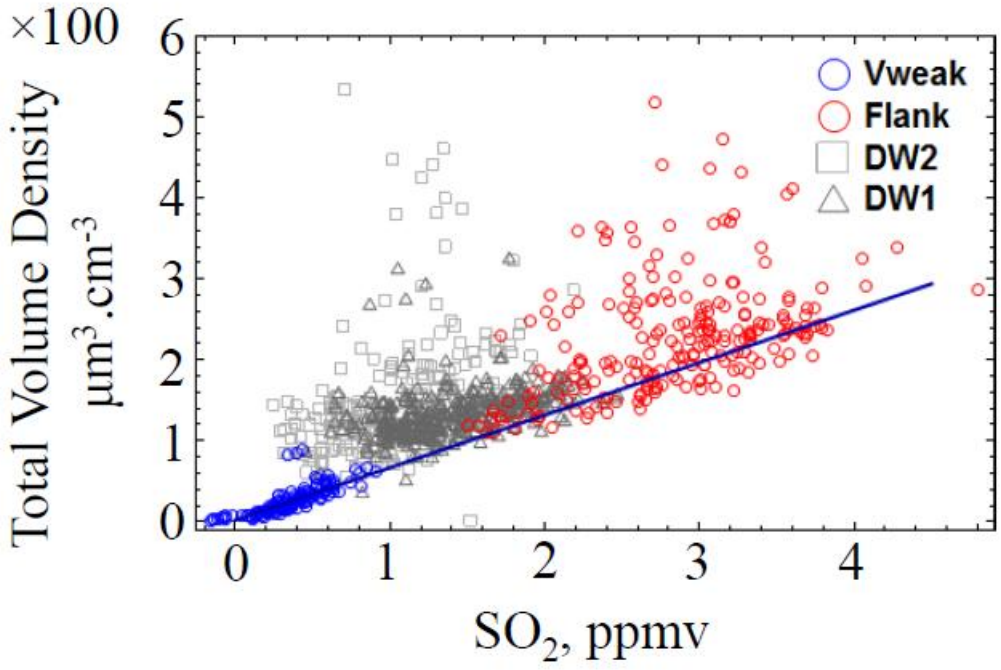

Figure 6

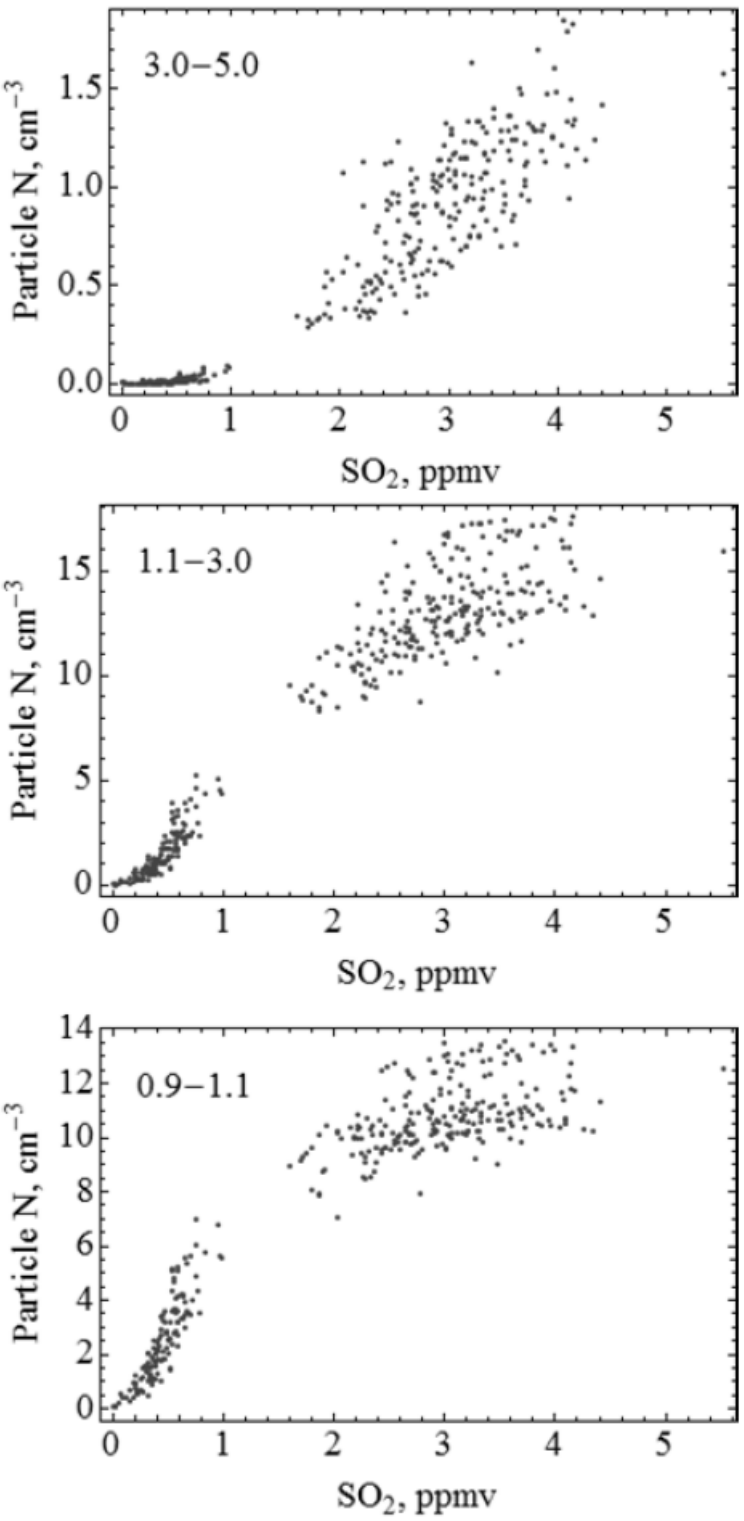
3.0–5.0
Particle N, cm^{-3}
SO$_2$, ppmv
1.1–3.0
Particle N, cm^{-3}
SO$_2$, ppmv
0.9–1.1
Particle N, cm^{-3}
SO$_2$, ppmv

Figure 7

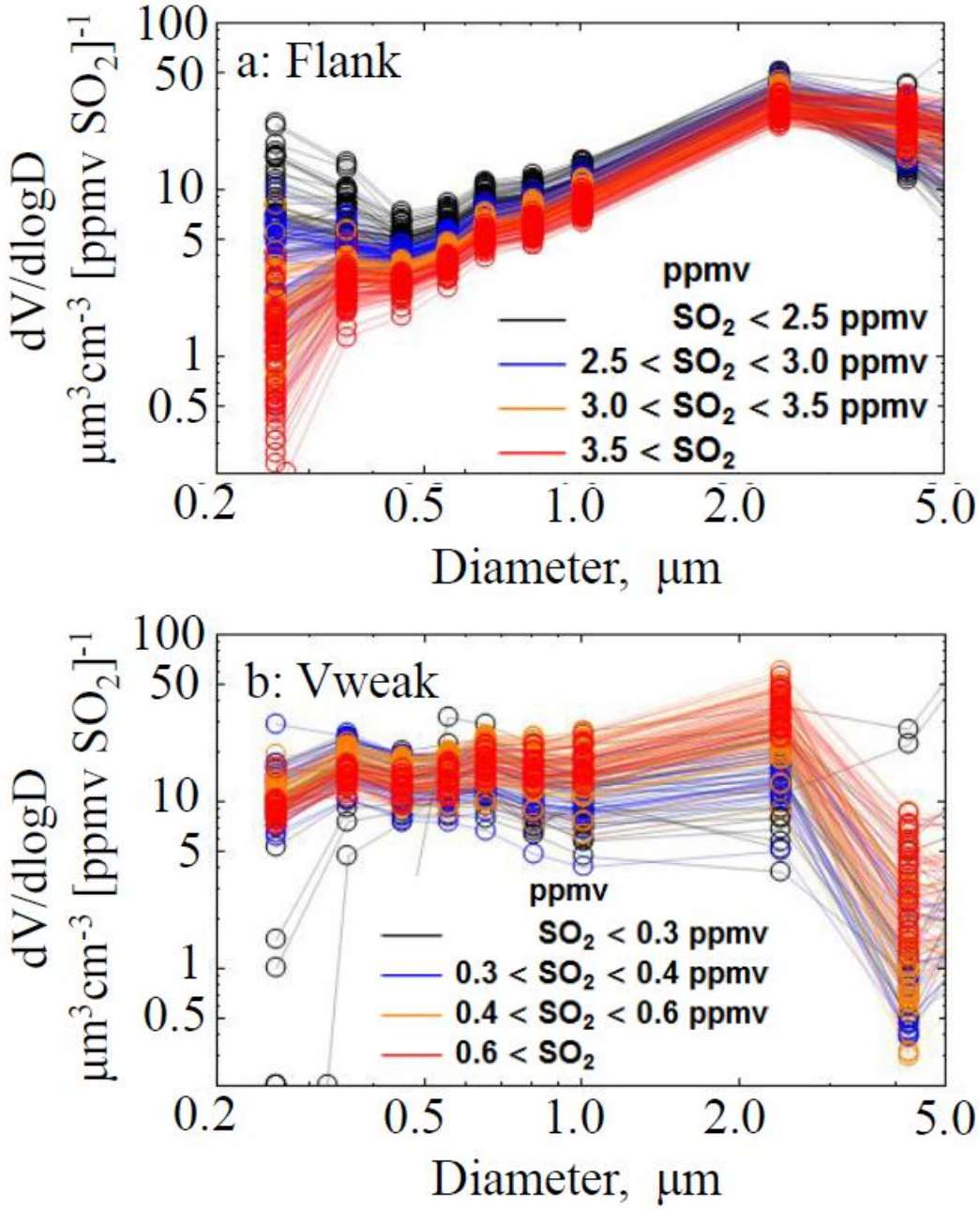
a: Flank
dV/dlogD
µm³cm⁻³ [ppmv SO₂]⁻¹
100
50
10
5
1
0.5
0.2
0.5
1.0
2.0
5.0
Diameter, µm
ppmv
SO₂ < 2.5 ppmv
2.5 < SO₂ < 3.0 ppmv
3.0 < SO₂ < 3.5 ppmv
3.5 < SO₂
b: Vweak
dV/dlogD
µm³cm⁻³ [ppmv SO₂]⁻¹
100
50
10
5
1
0.5
0.2
0.5
1.0
2.0
5.0
Diameter, µm
ppmv
SO₂ < 0.3 ppmv
0.3 < SO₂ < 0.4 ppmv
0.4 < SO₂ < 0.6 ppmv
0.6 < SO₂

Figure 8

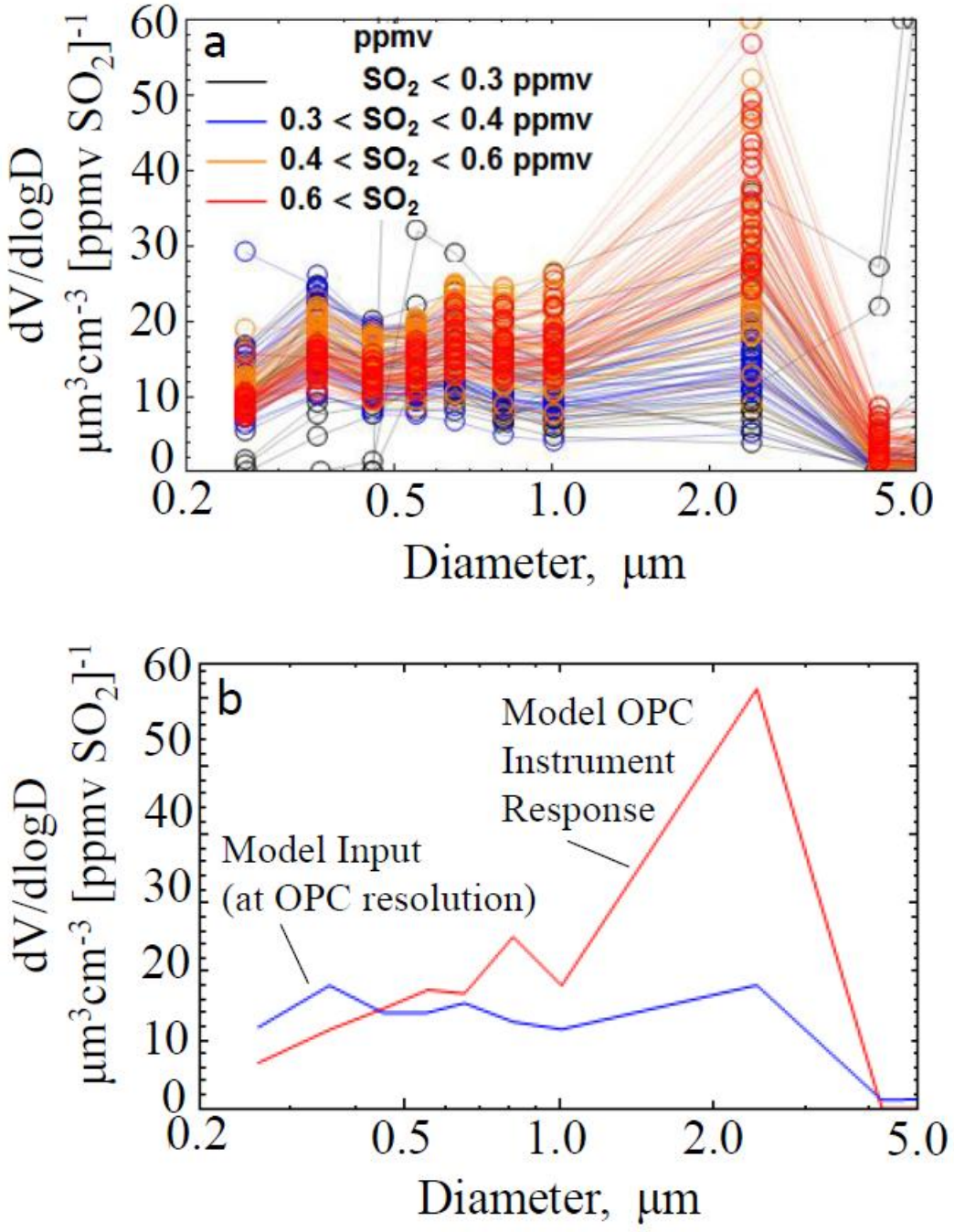
a
ppmv
SO2 < 0.3 ppmv
0.3 < SO2 < 0.4 ppmv
0.4 < SO2 < 0.6 ppmv
0.6 < SO2
dV/dlogD
µm3cm-3 [ppmv SO2]-1
Diameter, µm
b
Model OPC
Instrument
Response
Model Input
(at OPC resolution)
dV/dlogD
µm3cm-3 [ppmv SO2]-1
Diameter, µm

Figure 9

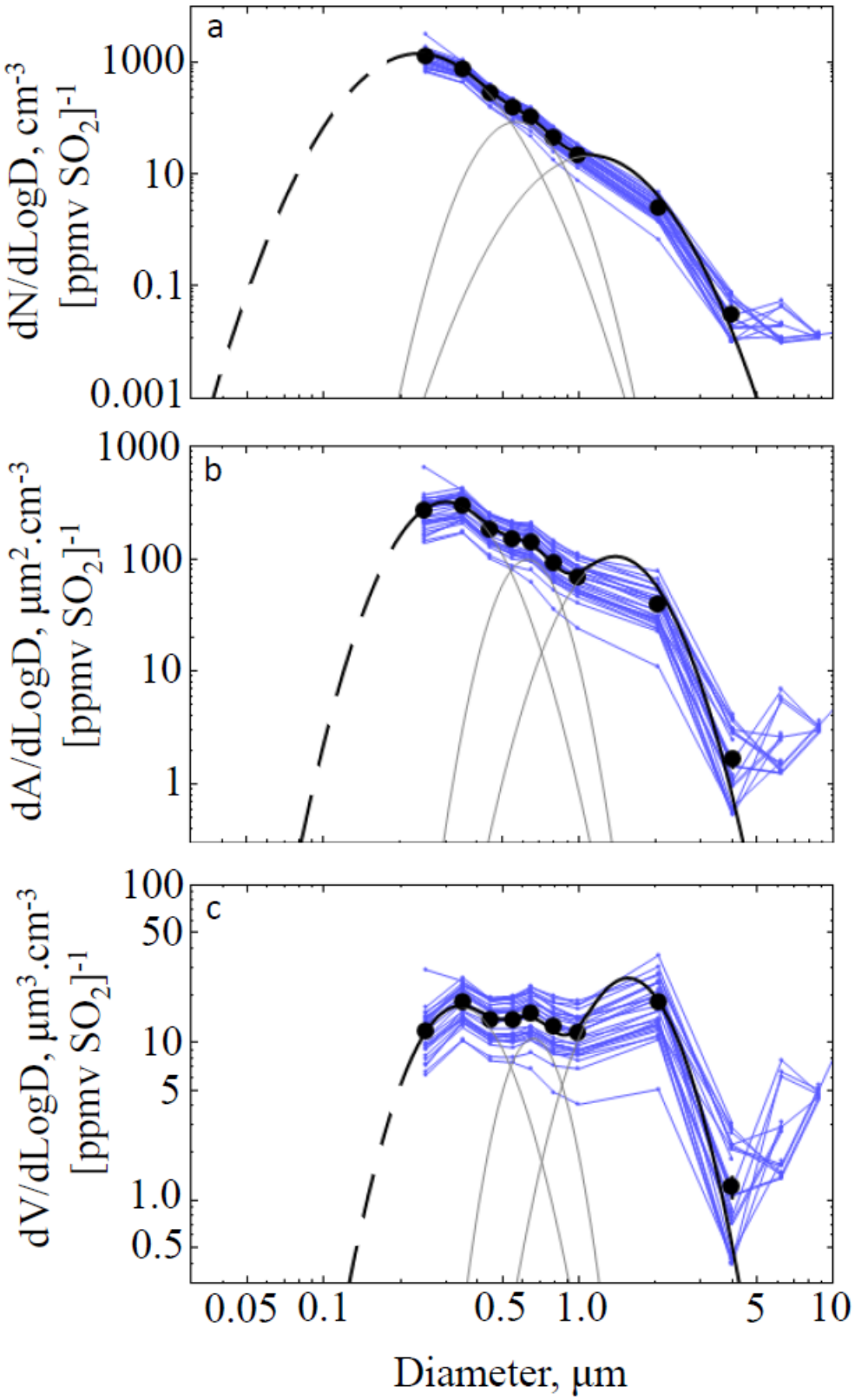
a
b
c
dN/dLogD, cm-3 [ppmv SO2]-1
dA/dLogD, µm2.cm-3 [ppmv SO2]-1
dV/dLogD, µm3.cm-3 [ppmv SO2]-1
1000
10
0.1
0.001
100
1
50
5
1.0
0.5
0.05
0.1
0.5
1.0
5
10
Diameter, µm

Figure 10

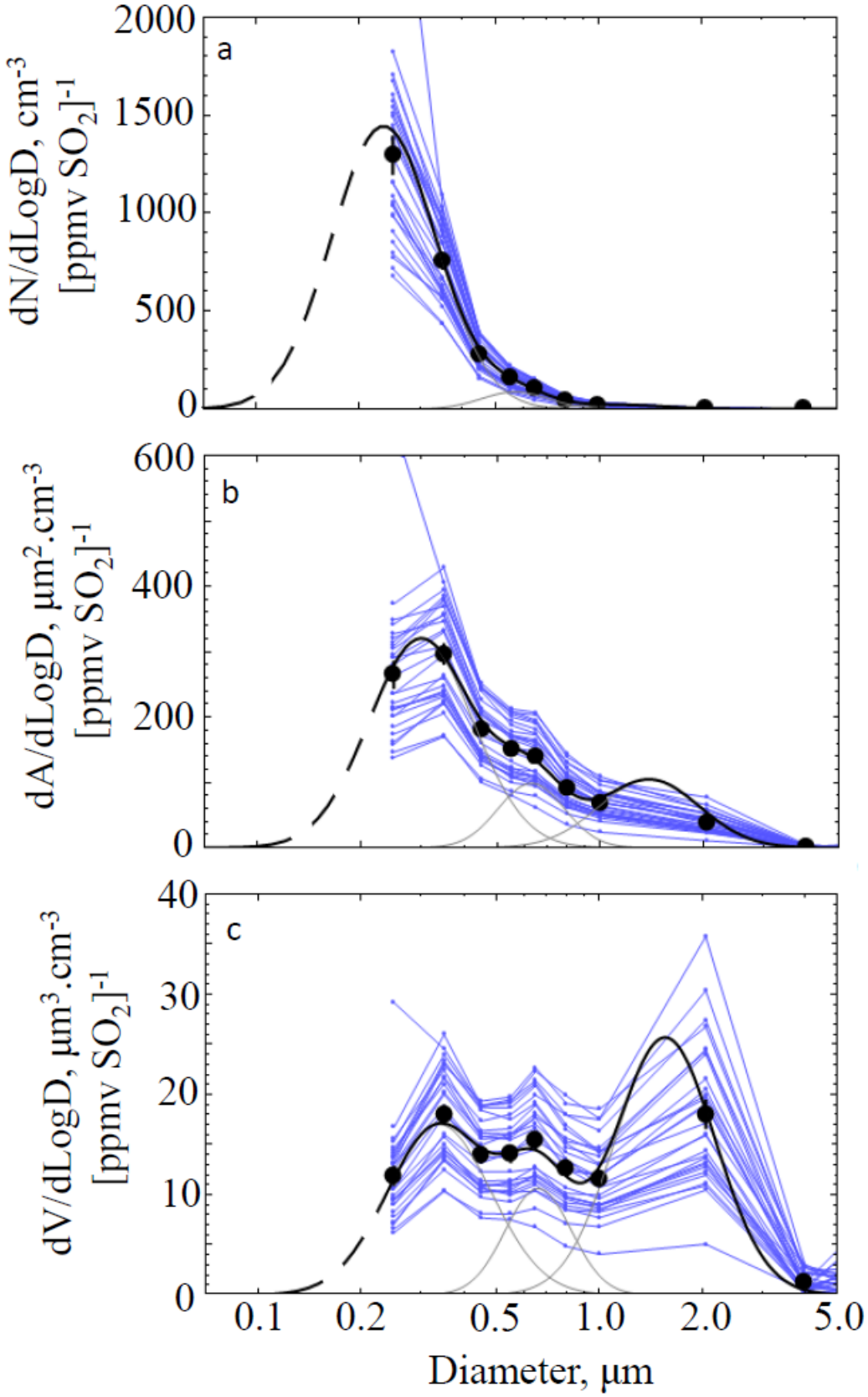
a
b
c
dN/dLogD, cm-3 [ppmv SO2]-1
dA/dLogD, µm2.cm-3 [ppmv SO2]-1
dV/dLogD, µm3.cm-3 [ppmv SO2]-1
2000
1500
1000
500
0
600
400
200
0
40
30
20
10
0
0.1
0.2
0.5
1.0
2.0
5.0
Diameter, µm

Figure 11

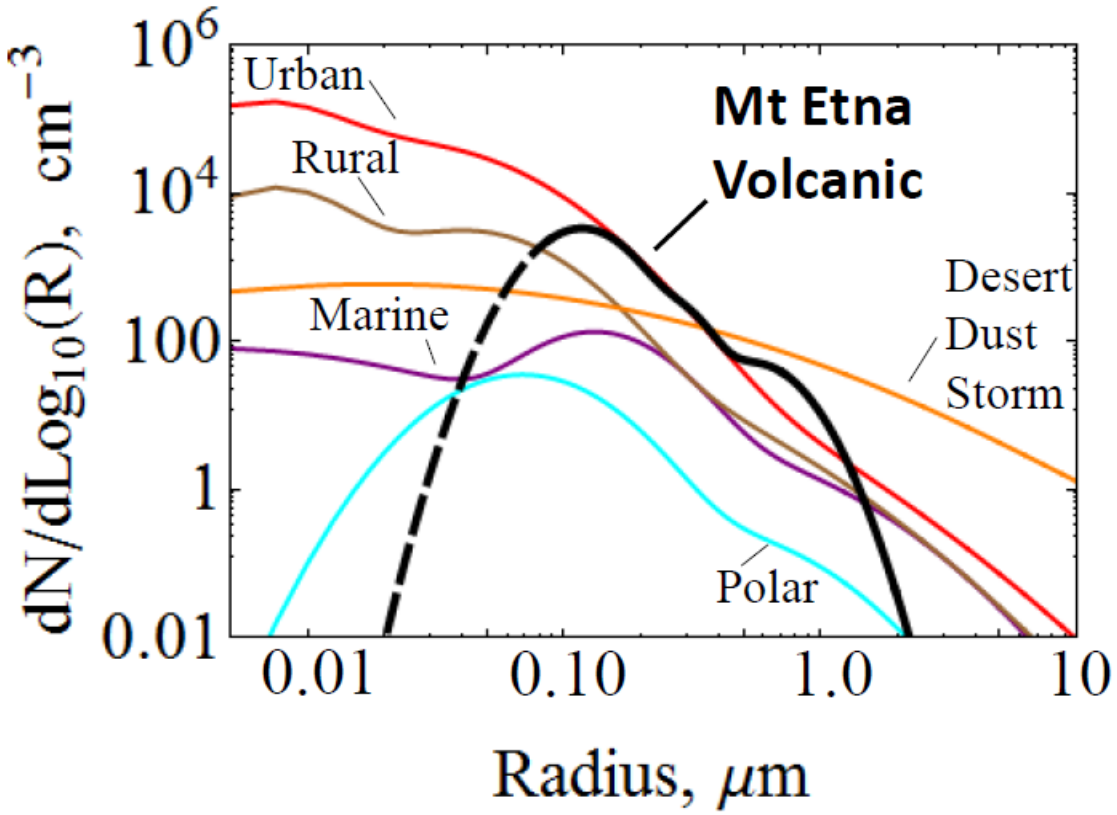

Figure 12

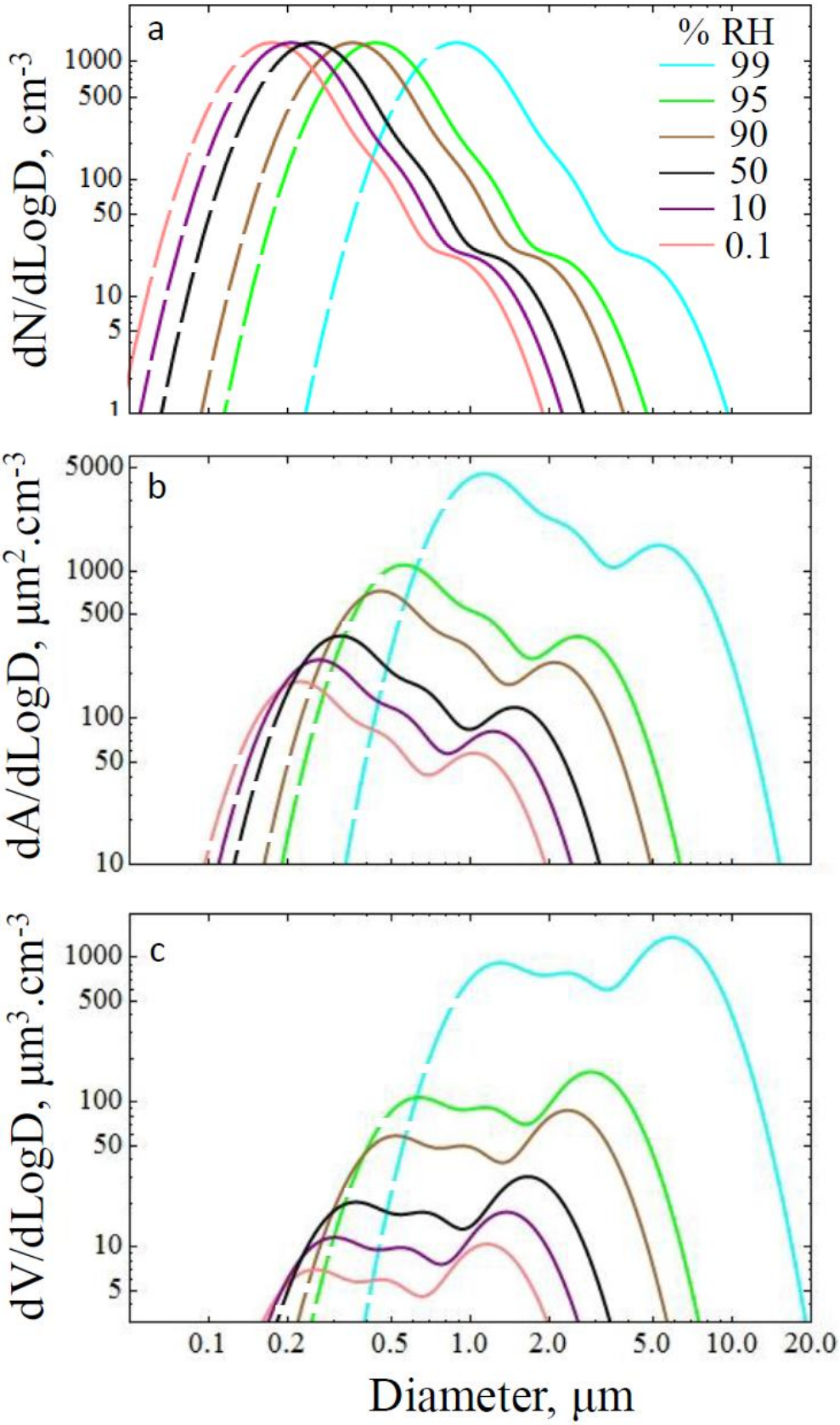
a
% RH
99
95
90
50
10
0.1
dN/dLogD, cm-3
1000
500
100
50
10
5
1
b
dA/dLogD, µm2.cm-3
5000
1000
500
100
50
10
c
dV/dLogD, µm3.cm-3
1000
500
100
50
10
5
0.1
0.2
0.5
1.0
2.0
5.0
10.0
20.0
Diameter, µm

Figure 13

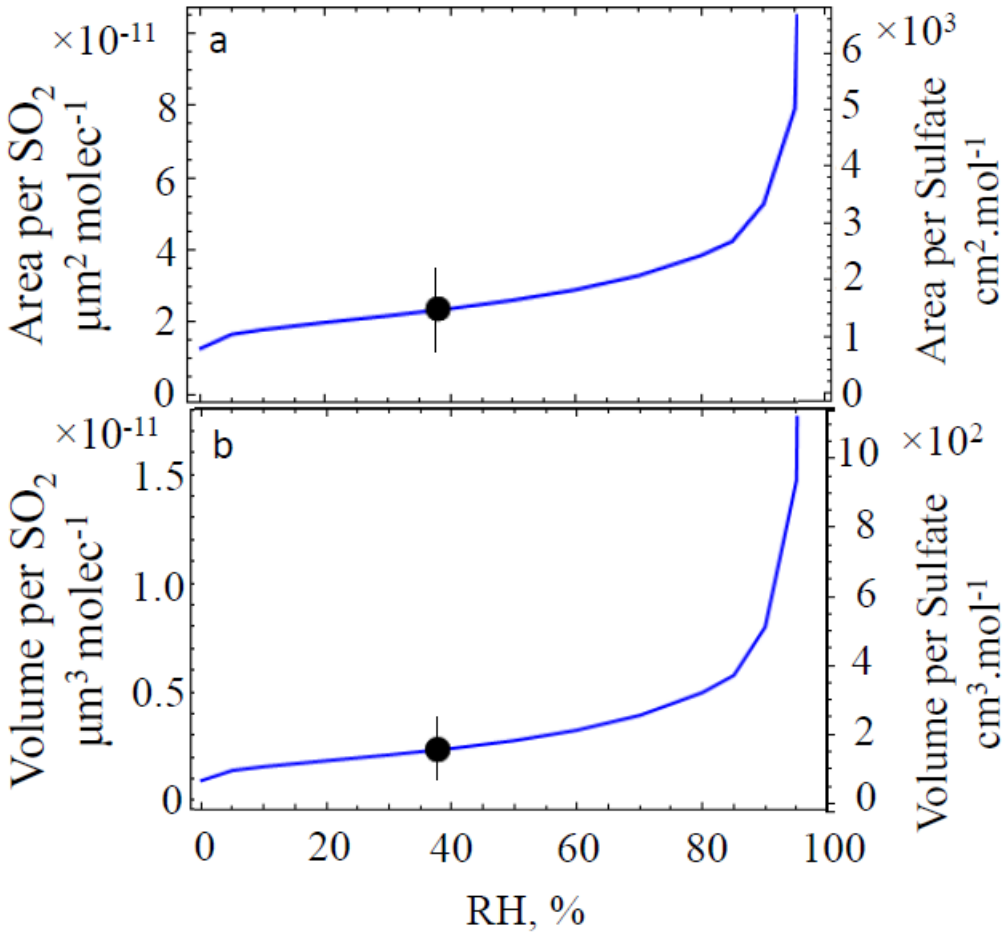

Figure 14

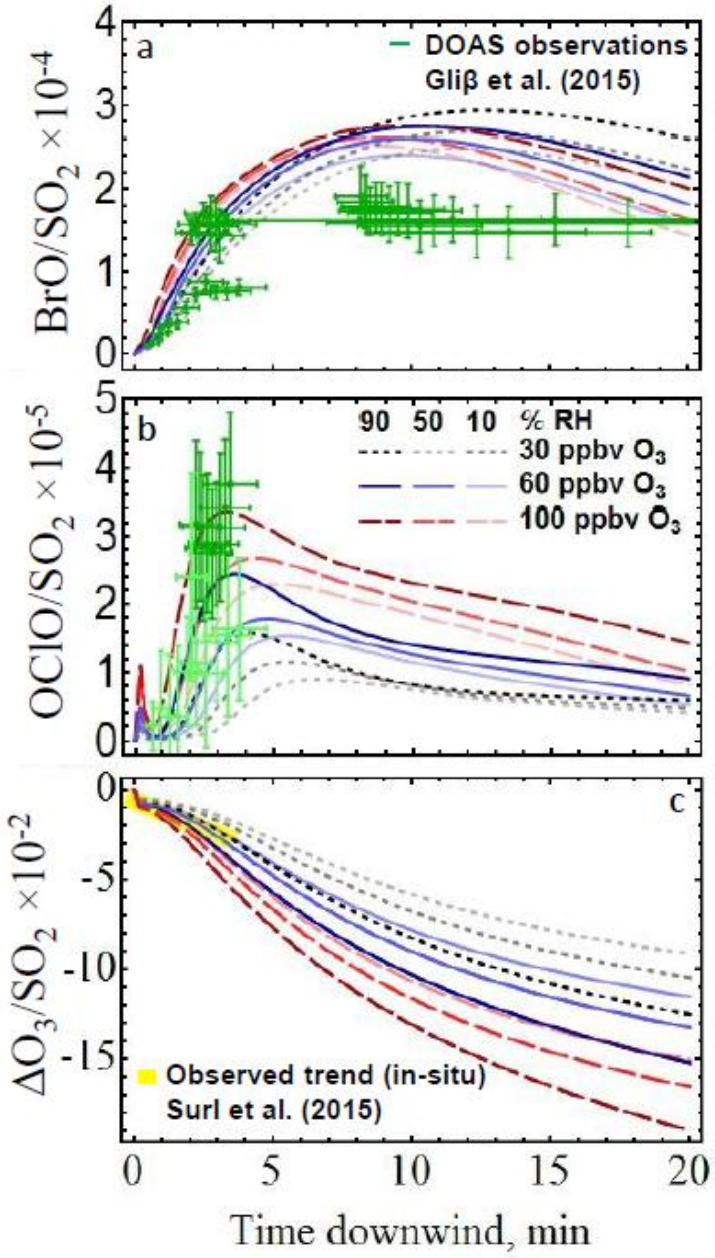
a
DOAS observations
Gliß et al. (2015)
BrO/SO2 ×10-4
b
90 50 10 % RH
30 ppbv O3
60 ppbv O3
100 ppbv O3
OClO/SO2 ×10-5
c
Observed trend (in-situ)
Surl et al. (2015)
ΔO3/SO2 ×10-2
Time downwind, min

Figure 15

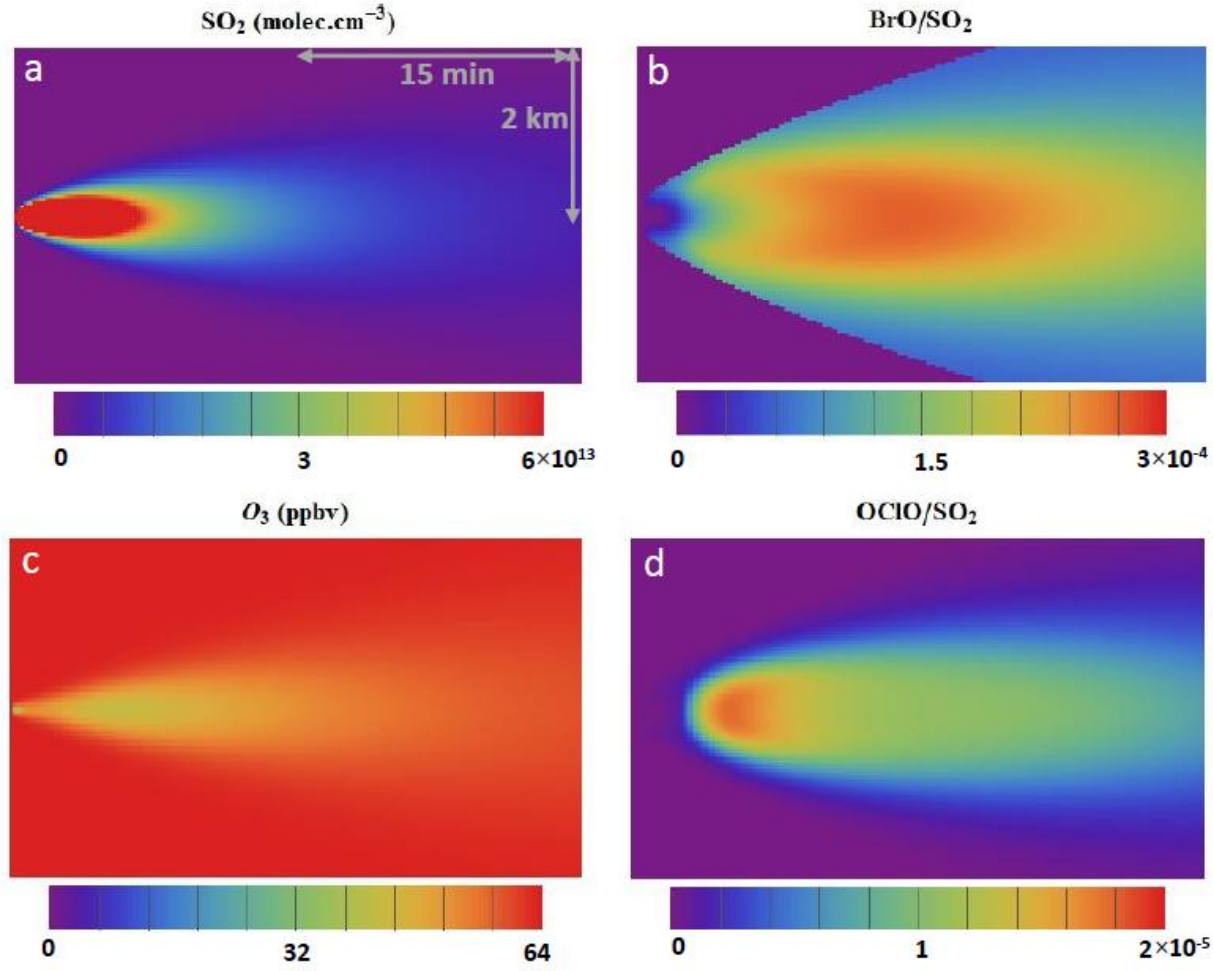

Figure 16

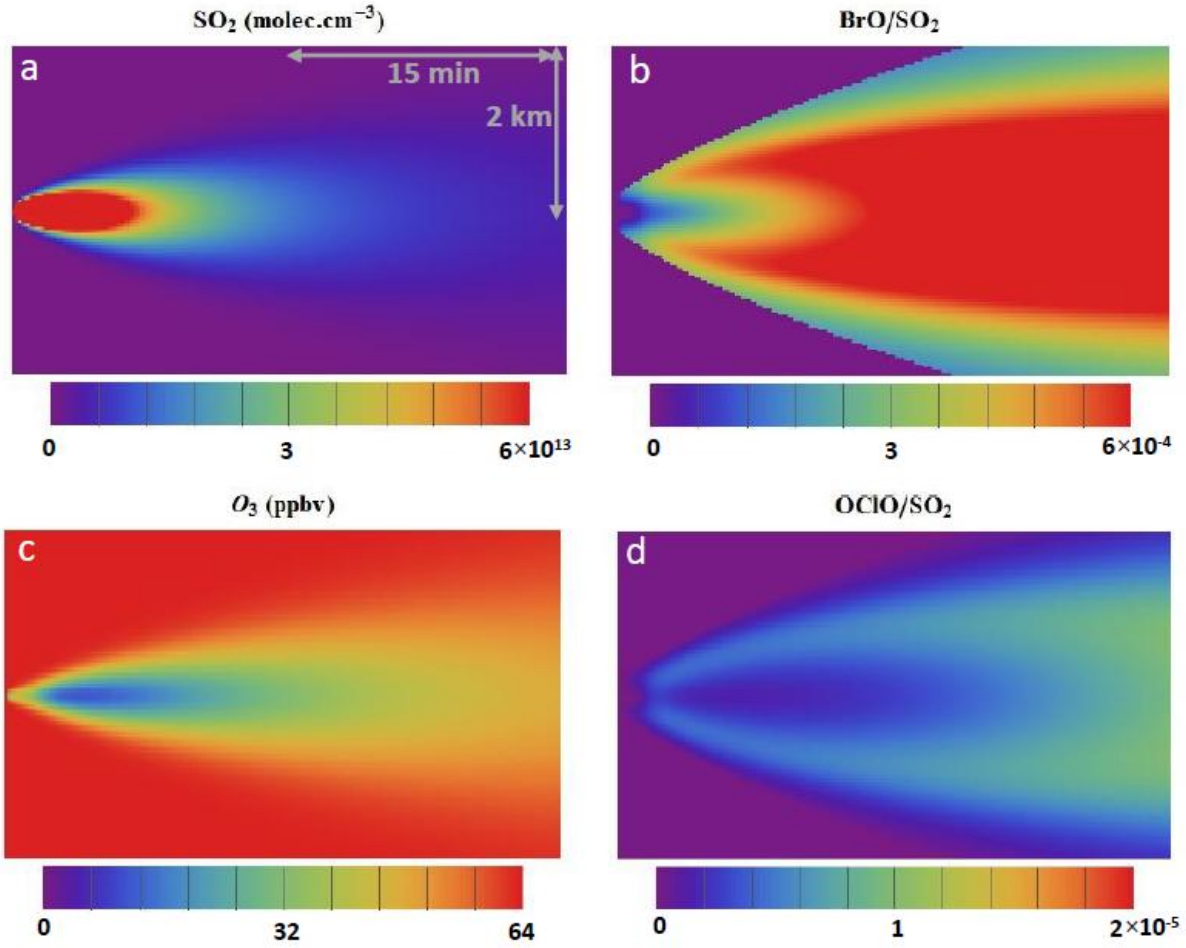

Figure 17

Table 1. Remote sensing observations of Mt Etna plume aerosol.

Remote Sensing Study	Methodology	Particle Size	Particle Flux	Particle Composition
Watson and Oppenheimer 2000	Sun-photometer (near source plume) Range: 0.1 to 4 µm radius	Tri-modal distributions with minima at 0.5 and 1.5 µm radius. Volume and Area distribution maxima lie beyond measurement range (at both large and small sizes) Effective radii (for observed range): 0.83 µm	4.5 – 8 kg s^{-1} (over measurement range only i.e. lower limit. Calculated using typical plume width, gas flux, assumed $H_2SO_{4(aq)}$/water densities)	Not characterised but Sulfate/water assumed for small/large particles
Watson and Oppenheimer 2001	Sun-photometer(near source plume) Range: 0.1 to 4 µm radius	Bi-/uni-modal distributions. Volume and Area distribution maxima lie beyond measurement range (at both large and small sizes) Effective radii: 1.5 (ash-rich), 0.7 (no ash) µm	-	-
Spinetti and Buongiorno, 2007	Airborne multispectral images (eruption and quiescent degassing)	Explosive phase shows larger particles whilst quiescent phase dominated by particles with ~1 µm effective radius.	-	-
Scollo et al., 2012	MISR (Multiangle Imaging SpectroRadiometer) satellite instrument (eruption events)	Large and fine particles depending on volcanic activity	-	Ash-dominated particles larger than sulfate/water
Sellitto et al. 2016	Sun-photometer/CIMEL at Lampedusa (transported, aged eruption plume) Range 0.06 to 10 µm diameter. Brewer Dobson MK III for column SO_2	Bi-modal distributions with volume maxima at radii around 4 µm and 0.1-0.2 µm. SO_2 close to detection limit, possible enhancements of 1-2 DU.	-	Large mode be likely ash, fine mode sulfate

Table 2. In-situ observations of Mt Etna plume aerosol, by time-averaged sampling and real-time techniques.

In-situ Study	Methodology	Particle Size	Particle Flux	Particle Composition
Vié le Sage et al. 1983	Cascade Impactor (Summit)	Sub-micron to supra-micron sizes	-	40 elements detected
Quisefit et al. 1988	Filter samplers (near-source, vents)	-	-	Particulate potassium
Ammann and Burtscher 1993, Ammann et al. 1993	Photoelectric charging of particles and TEM for fine particle detection	Ultrafine (nm) particles dominate number	-	Photoelectric activity related to Cu content in nm particles
Toutain et al. 1995	Filter samplers (near-source, vents)	-	-	Na, Al, Si, S, Cl K, Ca, Ti Fe, Mn, Cu, Zn
Allen et al. 2006	OPC (GRIMM 1.108, 1 min averaged) (summit & near-source plume) Range: 0.3 to 20 µm diameter Concurrent column SO_2 by DOAS. Filter-pack sampling: Coarse > 0.35 and fine < 0.35 µm diameter	Tri-modal number distributions with minima at ~1 and 3-4 µm. NEC (ash-rich) has more supramicron particles than VOR/BN (quiescently degassing). Area and Volume distributions not reported.	-	Sulfate-rich. Other ions include F^-, Cl^-, NO_3^-, Na^+, NH_4^+, K^+, Mg^{2+}, Ca^{2+}, H^+. Ash-rich NEC had greater mineral ion content. Sulfate mostly in coarse mode at NEC, fine mode at VOR/BN.
Martin et al.. 2008	Filter packs and cascade impactor: (summit & near-source plume) Range ~ 0.05 - 18 µm diameter Thermal precipitator (nm particles) Range: 4 - 40 nm	Sulphate ions at VOR/NEC: mono/bi-modal with maxima at 1 µm (and also 8 µm for NEC), size uncertainty due to flow rate variability. Silica: mono-modal with maximum ~1.4 µm by number distribution (~4 µm by volume). Elemental Sulfur and Sulfide: mono-modal with maximum ~ 1 µm	Sulfate flux not quantified. Silica flux: 10^{12} particles per second, ~7000 kg d^{-1}. Total nanoparticles ~10^{18} s^{-1}.	Sulfate (SO_4^{2-}) and Sodium (Na^+) as main ions, minor ions: F^-, Cl^-, Ca^{2+}, K^+, NH_4^+ Sulfate:SO_2 molar ratios of 0.017 - 0.05
Vance et al. 2010	In-situ OPC (TSI AeroTrak 8220) (summit & near-source plume) Range: 0.3 - 10 µm diameter	Coincidence errors affected measurement, lower limits reported. Total surface area: 4–78 cm^2 m^{-3} Number density: 75-860 cm^{-3}	-	-
Shcherbakov et al., 2016	Instrumented Aircraft, plume transects > 6km downwind. Polar Nephelometer, Forward Scattering Spectrometer probes	Number size distributions with effective radius 0.7-1.4 µm Differences in BN/NEC optical properties	-	Porous with air voids (estimated at 18-35 %)
Roberts et al., This study	In-situ OPC (LOAC: 0.1 Hz data) (summit & near-source plume) Range: 0.2 - 50 µm diameter Multi-Gas co-measured in-situ SO_2 SO_2 flux from DOAS-FLAME network	Particle volume well-correlated to SO_2. Coincidence errors traced. Tri-modal distribution exhibits volume maximum (~1-2 µm) within measurement range, area maximum at/beyond lower size-limit.	0.7 kg s^{-1} mass flux at measured RH (40%) and T (285 K), calculated using assumed $H_2SO_{4(aq)}$ or $NaHSO_{4(aq)}$ composition. 10^{16} s^{-1} number flux (lower limit)	No direct measurements. Analysis of volume:SO_2 assuming $H_2SO_{4(aq)}$/$NaHSO_{4(aq)}$ composition, yields estimated sulfate:SO_2 of 1-2 %

Table 3. Physical parameters measured during field campaign and calculated $H_2SO_{4(aq)}$ and $NaHSO_{4(aq)}$ properties.. The molar volume of $H_2SO_{4(aq)}$ is calculated at the observed temperature and Relative Humidity using parameterisations from Tabazadeh et al. (1997) for wt%H2SO4$_{(aq)}$ and density. The molar volume of $NaHSO_{4(aq)}$ is calculated at the observed Relative Humidity using parameterisations from Tang and Munkelwitz (1994) for wt%NaHSO4$_{(aq)}$ and density. See Appendix A1 for details.

Parameter	DW1	DW2	Flank	Vweak
Atmospheric density (molec.cm^{-3})	1.84×10^{19}	1.84×10^{19}	1.76×10^{19}	1.83×10^{19}
Temperature (˚C)	15.4	15.4 *	10.5	11.9 *
Relative Humidity (%)	49	49 *	21	38 *
Wt%H_2SO_4 (%) at RH and T	42	42	56	48
Density $H_2SO_{4(aq)}$ (g.cm^{-3}) at RH and T	1.33	1.33	1.47	1.39
Molar volume (cm^3.mol^{-1}) at RH and T	175	175	119	147
Wt%$NaHSO_4$ (%) at RH and T	67	67	85	75
Density $NaHSO_{4(aq)}$ (g.cm^{-3}) at RH and T	1.68	1.68	1.96	1.79
Molar volume (cm^3.mol^{-1}) at RH and T	107	107	72	89

**indicates humidity data measured shortly before selected time-period*

Table 4. Molar SO_4^{2-}:SO_2 ratios estimated from measured total particle volume and SO_2 time-series, assuming $H_2SO_{4(aq)}$ or $NaHSO_{4(aq)}$ composition, and molar volume (Table 3). Two sets of calculations are made, using the gradient of Figure 6 (direct analysis of Vweak plume measurements) or the lognormal distribution fitted to selected data optimised to minimise coincidence errors (see Table 5).

Parameter	Directly analysed Vweak	Lognormal Distribution (selected data)
Volume per ppmv SO_2 (µm^3.cm^{-3}.ppmv^{-1})	65	43
Atmospheric Density (molec.cm^{-3})	1.83E19	1.83E19
Volume per molecule SO_2 (µm^3.molec^{-1})	**3.5E-12**	**2.3E-12**
Volume per mole SO_2 (cm^3.mol^{-1})	**2.11**	**1.39**
Molar volume of $H_2SO_{4(aq)}$ (cm^3 mol^{-1})	147	147
Molar volume of $NaHSO_{4(aq)}$ (cm^3 mol^{-1})	89	89
SO_4^{2-}:SO_2 molar ratio ($H_2SO_{4(aq)}$)	**0.015**	**0.0095**
SO_4^{2-}:SO_2 molar ratio ($NaHSO_{4(aq)}$)	**0.024**	**0.016**

Table 5. Fitted tri-modal aerosol size distribution as plotted in Figures 11 and 12. This is optimal aerosol data from Vweak period, selected when $0.3 < SO_2 < 0.4$ ppmv and subsequently normalized to 1 ppmv SO_2. See text for details. Three parameters N, D and σ_g are provided that describe each fitted lognormal mode (see Appendix A3 for details). Volumetic parameter D_v is also given in brackets. Further parameters calculated from the lognormal fit include the effective radius, R_{eff}, the total number, area and volume integrated over the whole size distribution, and the percentage proportions of the individual three modes (1,2,3) to these totals. Aerosol/SO_2 ratios are finally calculated to derive fluxes (Section 3.4).

Parameter	
Volcanic aerosol submicron mode 1:	
N1 (cm^{-3})	1266
D1 (µm)	0.235 (0.34)
σ_g1	1.42
Volcanic aerosol medium mode 2:	
N2 (cm^{-3})	49
D2 (µm)	0.57 (0.66)
σ_g2	1.25
Volcanic aerosol supramicron mode 3:	
N3 (cm^{-3})	18.2
D3 (µm)	1.11 (1.56)
σ_g3	1.4
Calculated parameters from the model fit	
Volcanic R_{eff}, µm	0.30
Total Volcanic Number, Nt (cm^{-3})	1333
Total Volcanic Area, At ($\mu m^2.cm^{-3}$)	423
Total Volcanic Volume, Vt ($\mu m^3.cm^{-3}$)	43
Mode % contribution to number (1,2,3)	95, 4, 1
Mode % contribution to area (1,2,3)	66, 13, 21
Mode % contribution to volume (1,2,3)	35, 14, 51
Co-measured in-situ parameters	
SO_2 (normalized) ppmv	1
Atmospheric Density ($molec.cm^{-3}$)	1.83×10^{19}
SO_2 concentration (normalized) ($molec^{-1}.cm^{-3}$)	1.83×10^{13}
Temperature (˚C)	11.9
Relative Humidity (%)	38
Calculated Aerosol/SO_2 ratios	
Number/SO_2 (particles $molec^{-1}$)	7.3×10^{-11}
Area/SO_2 (μm^2 $molec^{-1}$)	2.3×10^{-11}
Volume/SO_2 (μm^3 $molec^{-1}$)	2.4×10^{-12}
SO_2 gas flux by remote sensing	
Minimum (t d^{-1})	1800
Maximum (t d^{-1})	2100
Mean (t d^{-1})	1950
Mean Aerosol fluxes	
Particle Number (lower limit) (s^{-1})	1.5×10^{16}
Surface Area (μm^2 s^{-1})	4.9×10^{15}
Volume (μm^3 s^{-1})	5.0×10^{14}